

Multifractal-enriched mobility edges and emergent quantum phases in one-dimensional exactly solvable lattice models

Shan-Zhong Li,^{1,2} Yi-Cai Zhang,³ Yucheng Wang,⁴ Shanchao Zhang,^{1,2,5} Shi-Liang Zhu,^{1,2,5,*} and Zhi Li^{1,2,†}

¹Key Laboratory of Atomic and Subatomic Structure and Quantum Control (Ministry of Education), Guangdong Basic Research Center of Excellence for Structure and Fundamental Interactions of Matter, School of Physics, South China Normal University, Guangzhou 510006, China

²Guangdong Provincial Key Laboratory of Quantum Engineering and Quantum Materials, Guangdong-Hong Kong Joint Laboratory of Quantum Matter, Frontier Research Institute for Physics, South China Normal University, Guangzhou 510006, China

³School of Physics and Materials Science, Guangzhou University, Guangzhou 510006, China

⁴Shenzhen Institute for Quantum Science and Engineering,

Southern University of Science and Technology, Shenzhen 518055, China

⁵Quantum Science Center of Guangdong-Hong Kong-Macao Greater Bay Area, Shenzhen, China

We propose a class of exactly solvable flat-band quasiperiodic lattice models that encompass a variety of multifractal-enriched mobility edges and multi-state coexisting quantum phases. Utilizing Avila's global theory, we derive exact expressions of the Lyapunov exponents in both lattice and dual spaces, providing an analytical expression and phase diagram for the multifractal-enriched mobility edges. Additionally, we numerically compute the inverse participation ratios of the eigenstates in both real and dual spaces to further characterize these phases. Furthermore, we demonstrate that these models can be realized using Rydberg atomic arrays, enabling the observation of Lyapunov exponents and inverse participation ratios through a powerful spectroscopy approach.

Introduction.— Anderson localization elucidates a fundamental principle concerning how disorder induces a metal-insulator phase transition [1]. Furthermore, three-dimensional disorder systems and even one-dimensional quasiperiodic lattices [2] may exhibit phases where extended and localized states coexist, with a mobility edge (ME) distinguishing between them [3]. Additionally, in quasiperiodic systems, a third fundamental state known as the multifractal state emerges [4, 5]. The energy level statistics [6, 7], wave function distributions [8, 9], and dynamical properties [10, 11] of the multifractal state significantly differ from those of localized and extended states. Recent studies indicate that the multifractal state may enhance the superconducting transition temperature [12–16].

The discovery of multifractal states has significantly broadened our understanding of MEs. Subsequent research has sought to identify multifractal-enriched mobility edges (MMEs), which delineate the multifractal states from either extended or localized states [17–29]. However, much of the work on MMEs relies on numerical analyses, which often involve tedious scaling assessments [18–24]. Currently, two primary approaches have been proposed for achieving exact MMEs: the introduction of unbounded potential [25–28] and the utilization of incommensurate hopping [29]. Both methods facilitate the conversion of energy into a singular continuous spectrum [29, 30], thus inducing the ME that distinguishes the multifractal state from the localized state. Additionally, recent work has examined a specific quasiperiodic lattice with long-range hopping through dual transformations and renormalization group techniques [31, 32], revealing MMEs and a coexistence of three distinct quan-

tum phases. Despite considerable efforts in researching MMEs [17–29, 31], the question remains unresolved: Is there a universal platform capable of inducing all types of MMEs and facilitating the exploration of all conceivable multi-state coexisting quantum phases? These states are typically characterized by Lyapunov exponents (LEs) and inverse participation ratios (IPRs). An equally important question arises: How can we experimentally realize MMEs and identify a suitable method for detecting LEs and IPRs?

In this Letter, we address these challenges by introducing a class of flat-band lattices, wherein a complete set of MMEs and emergent quantum phases exist, with analytical expressions derivable through Avila's global theorem [33]. Furthermore, we demonstrate that these models can be realized in artificial quantum systems, and that reliable indicators such as LEs and IPRs can be detected using a powerful spectroscopy approach.

The Diamond Lattice Model and Main Results.—We analytically demonstrate that MMEs can arise in a class of flat-band models featuring partially quasiperiodic modulation (see Supplementary Materials (SM) [34]). As a representative example, we here utilize a diamond lattice [35] shown in Fig. 1(a) to illustrate our ideas, and the Hamiltonian of this model reads

$$H_D = \sum_{n=1}^N (J a_n^\dagger b_n + J a_n^\dagger c_n + t b_n^\dagger c_n + \text{H.c.}) + \sum_{n=1}^{N-1} (J b_n^\dagger a_{n+1} + J c_n^\dagger a_{n+1} + \text{H.c.}) + \sum_{n=1}^N V_n c_n^\dagger c_n, \quad (1)$$

where a_n (a_n^\dagger), b_n (b_n^\dagger), and c_n (c_n^\dagger) are the annihilation (creation) operators corresponding to sublattices A,

B , and C in the n -th primitive cell, respectively. The quantities J and t denote the hopping strengths between the A and B/C sublattices and between the B and C sublattices, respectively. Here, N denotes the total number of primitive cells. A quasiperiodic potential, defined as $V_n = 2\lambda \cos(2\pi\alpha n + \theta)$, is applied solely to sublattice C , where λ , α , and θ represent the strength of the quasiperiodic potential, an irrational number, and a phase offset, respectively. When $\lambda = 0$, Hamiltonian (1) showcases a perfect flat band characterized by $E_k = -t$ along with two dispersive bands given by $E_k = (t \pm \sqrt{16J^2 \cos(k) + 16J^2 + t^2})/2$ [35].

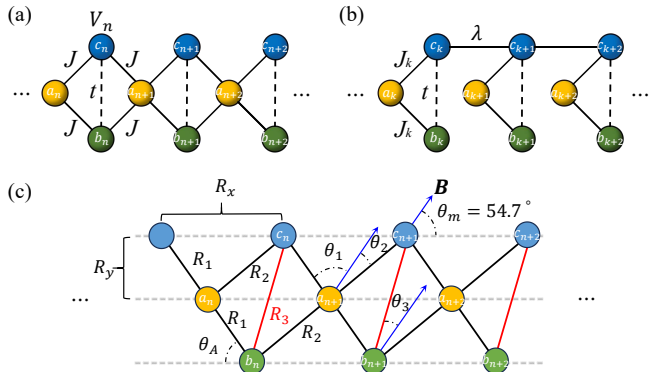


FIG. 1. The diamond lattice model represented in (a) lattice space, (b) dual space, (c) and its experimental implementation with Rydberg atomic array.

To accurately derive the MEs of Hamiltonian (1), we employ a dual space as an auxiliary framework. By applying the dual transformations $a_n = \frac{1}{\sqrt{N}} \sum_k a_k e^{-i2\pi\alpha kn}$, $b_n = \frac{1}{\sqrt{N}} \sum_k b_k e^{-i2\pi\alpha kn}$, and $c_n = \frac{1}{\sqrt{N}} \sum_k c_k e^{-i2\pi\alpha kn}$ for $\theta = 0$, we can derive the corresponding Hamiltonian in dual space:

$$H_K = \sum_{k=1}^N (J_k a_k^\dagger b_k + J_k a_k^\dagger c_k + \text{H.c.}) + \sum_{k=1}^N (t b_k^\dagger c_k + \text{H.c.}) + \sum_{k=1}^{N-1} (\lambda c_{k+1}^\dagger c_k + \text{H.c.}), \quad (2)$$

where $J_k = J + J e^{i2\pi\alpha k}$. The geometric structure (refer to Fig. 1(b)) illustrates that the system operates as an extended Fano defect quasiperiodic lattice in dual space [35]. For the purpose of numerical calculations, we set $J = 1$ as the energy unit and impose periodic boundary conditions. The additional parameters are $\theta = 0$ and $\alpha = \lim_{m \rightarrow \infty} \frac{F_{m-1}}{F_m} = (\sqrt{5} - 1)/2$, where F_m denotes the m -th Fibonacci number. In finite-size studies, we specify the system size as $N = F_m$ and $\alpha = F_{m-1}/F_m$ to maintain accurate periodic boundary conditions. The MEs of Hamiltonian (1) can be categorized into two scenarios: $t < 2$ and $t \geq 2$. Given the similarity of outcomes in both cases, we present only the results for $t < 2$ in the

main text (see SM [34] for the $t \geq 2$ case).

The primary findings of our analysis indicate that a comprehensive set of MMEs and all possible coexisting quantum phases can emerge within a class of flat-band models featuring partially quasiperiodic modulations. Furthermore, these predictions are readily demonstrable in current artificial quantum systems.

The universal analytical expressions for the MMEs and the potential quantum phases of model (1) are consolidated in Table I. To facilitate comprehension of the universal expressions presented in this table, we depict results for a specific case in Fig. 2, which delineates three distinct regions. In the region $\lambda \leq 1$, we identify two types of MEs: one being a traditional ME that distinguishes between localized and extended states, and the other an MME that differentiates multifractal from extended states. In the region $1 < \lambda < 3$, we observe three types of MEs: one separating localized and extended states, another MME separating multifractal and extended states, and the third MME distinguishing multifractal from localized states. Finally, in the region $\lambda \geq 3$, only a single type of MME exists, effectively separating localized states from multifractal states, while the corresponding multi-state coexisting quantum phases also arise.

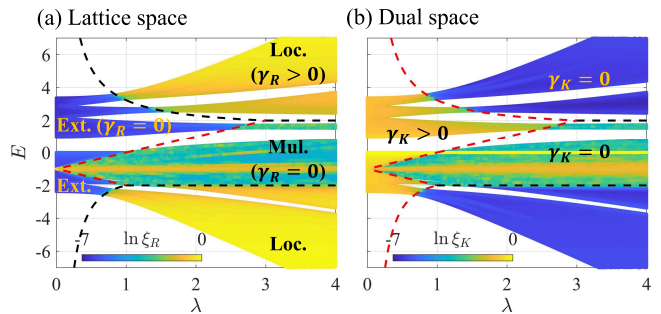


FIG. 2. Phase diagram of the diamond lattice model. (a) The lattice space IPR ξ_R and (b) the dual space IPR ξ_K as functions of potential strength λ and energy E . The phase boundaries, marked by dashed lines, are determined from the critical energies that have been exactly solved. The parameters $N = 377$ and $t = 1$.

Analytical expressions of the LEs.— Lyapunov exponents are essential for characterizing localization properties in quantum systems. We now demonstrate that the LEs for the diamond lattice model can be analytically derived using Avila's global theory [33]. The $\gamma_{R(K)}$ defined as the LE of the eigenstate associated with the eigenvalue E in lattice (dual) space can be obtained from

$$\gamma_{R(K)} = \lim_{N \rightarrow \infty} \frac{1}{N} \ln \left\| \prod_{n(k)=1}^N T_{n(k)} \right\|, \quad (3)$$

where $\|\cdot\|$ denotes the matrix norm, and $T_{n(k)}$ represents the transfer matrix. The properties of the LEs are summarized in Table II [28].

TABLE I. MMEs and emergent quantum phases of model (1) under the condition of $t < 2$

Disorder strength	$\lambda \leq 2 - t$		$2 - t < \lambda < 2 + t$			$\lambda \geq 2 + t$
Exact MMEs ($E_c =$)	$\pm \frac{1}{\lambda} \pm \sqrt{\frac{1}{\lambda^2} \pm \frac{2t}{\lambda} + 2}$	$\pm \lambda - t$	$\frac{1}{\lambda} + \sqrt{\frac{1}{\lambda^2} + \frac{2t}{\lambda} + 2}$	$\lambda - t$	-2	± 2
Separated states	Ext.* and Loc.	Ext. and Mul.	Ext. and Loc.	Ext. and Mul.	Ext. and Mul.	Loc. and Mul.
Quantum phases	Ext.+Mul.; Ext.+Mul.+Loc.		Ext.+Mul.+Loc.			Loc.+Mul.

*Ext.=Extended states; Loc.=Localized states; Mul.=Multifractal states.

TABLE II. Key indicators of states' localization feature

States	LEs	IPRs
Ext.	$\gamma_R = 0$ & $\gamma_K > 0$	$\xi_R \sim 1/3N$ & $\xi_K(E) \sim \mathcal{O}(1)$
Loc.	$\gamma_R > 0$ & $\gamma_K = 0$	$\xi_R \sim \mathcal{O}(1)$ & $\xi_K \sim 1/3N$
Mul.	$\gamma_R = 0$ & $\gamma_K = 0$	$1/3N < \xi_R \approx \xi_K < \mathcal{O}(1)$

The LE in lattice space is mathematically determined by the eigenequation of the Hamiltonian (1)

$$\begin{aligned}
\psi_{b,n-1} + \psi_{c,n-1} + \psi_{b,n} + \psi_{c,n} &= E\psi_{a,n}, \\
\psi_{a,n+1} + \psi_{a,n} + t\psi_{c,n} &= E\psi_{b,n}, \\
\psi_{a,n+1} + \psi_{a,n} + t\psi_{b,n} + V_n\psi_{c,n} &= E\psi_{c,n}.
\end{aligned} \tag{4}$$

By simplifying the equations, one can get

$$\begin{aligned}
\psi_{c,n+1} &= \frac{E^3 - (E^2 - 2)V_n - t^2E - 4(E+t)}{2(E+t) - V_{n+1}} \psi_{c,n} \\
&\quad - \frac{2(E+t) - V_{n-1}}{2(E+t) - V_{n+1}} \psi_{c,n-1}.
\end{aligned} \tag{5}$$

By extracting coefficients, one can obtain the corresponding transfer matrix as $T_n = A_n B_n$, where $A_n = 1/M_{n+1}$ and

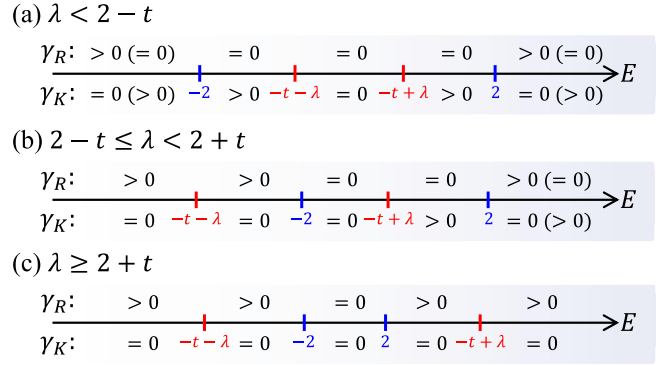
$$B_n = \begin{pmatrix} E^3 - (E^2 - 2)V_n - t^2E - 4(E+t) & -M_{n-1} \\ M_{n+1} & 0 \end{pmatrix}$$

with $M_n = 2(E+t) - V_n$. Utilizing Avila's global theory [33], we derive analytical expressions for the LEs in terms of the eigenvalue E in lattice space. Similarly, we can also obtain the analytical LEs in dual space. The complete expressions for the LEs can be written as

$$(\gamma_R, \gamma_K) = \begin{cases} (\gamma_{R,1}, \gamma_{K,1}), & |E+t| > \lambda \text{ \& \ } |E^2 - 2| > 2, \\ (\gamma_{R,2}, 0), & |E+t| \leq \lambda \text{ \& \ } |E^2 - 2| > 2, \\ (0, \gamma_{K,2}), & |E+t| > \lambda \text{ \& \ } |E^2 - 2| \leq 2, \\ (0, 0), & |E+t| \leq \lambda \text{ \& \ } |E^2 - 2| \leq 2, \end{cases} \tag{6}$$

where $\gamma_{R,1} = \max \left\{ \ln \left| \frac{\lambda c_1}{2c_2} \right|, 0 \right\}$, $\gamma_{R,2} = \ln \left| \frac{c_1}{2} \right|$, $\gamma_{K,1} = \max \left\{ \ln \left| \frac{2c_2}{\lambda c_1} \right|, 0 \right\}$ and $\gamma_{K,2} = \ln \left| \frac{c_1}{\lambda} \right|$ with $c_1 = |E^2 - 2| + \sqrt{(E^2 - 2)^2 - 4}$ and $c_2 = |E+t| + \sqrt{(E+t)^2 - \lambda^2}$ [34].

Phase diagram determined by the analytical LEs.— We now demonstrate that the MMEs and the emergent quantum phases listed in Table I, as well as the phase boundaries represented by dashed lines in Fig. 2, can be derived from the analytical expressions presented in Eq. (6). Mathematically, the inequality involving the absolute value yields two critical points. Consequently, each line in Eq. (6) results in four critical points ($E_c = -2, -t - \lambda, -t + \lambda, 2$), which partition the energy axis into five distinct regions, as shown in Fig. 3.

FIG. 3. Phase diagram versus E for various λ .

A specific value of λ results in three distinct relationships concerning the relative positions of the four critical points: $-2 \leq -t - \lambda < -t + \lambda < 2$, $-t - \lambda < -2 < -t + \lambda < 2$, and $-t - \lambda < -2 < 2 \leq -t + \lambda$. Therefore, the discussion of the LEs must be divided into three cases: ① $\lambda \leq 2 - t$ [Fig. 3(a)], ② $2 - t < \lambda < 2 + t$ [Fig. 3(b)], and ③ $\lambda \geq 2 + t$ [Fig. 3(c)].

We can further derive the values of the LEs using the inequalities in Eq. (6). Case ① [see Fig. 3(a)]: In the regions where $E < -2$ or $E > 2$, we obtain the pairs $(\gamma_R, \gamma_K) = (\gamma_{R,1}, \gamma_{K,1})$ from the inequalities $|E+t| > \lambda$ and $|E^2 - 2| > 2$ presented in the first line of Eq. (6). Consequently, only extended states ($\gamma_R = 0$ and $\gamma_K > 0$) or localized states ($\gamma_R > 0$ and $\gamma_K = 0$) can exist within this energy interval. We can further derive two traditional MEs by setting $\gamma_{R,1} = 0$: $E_c = \pm \frac{1}{\lambda} \pm \sqrt{\frac{1}{\lambda^2} \pm \frac{2t}{\lambda} + 2}$. Moreover, the fourth line of Eq. (6) indicates that $(\gamma_R, \gamma_K) = (0, 0)$ in the region

$-t - \lambda \leq E \leq -t + \lambda$, suggesting the emergence of multifractal states. Two corresponding MMEs can be identified: $E_c = \pm\lambda - t$. The remaining energy intervals can be analyzed similarly using the third and fourth lines of Eq. (6), leading to the conclusion that all eigenstates are extended. Thus, two-state (Extended + Multifractal) and three-state (Extended + Multifractal + Localized) coexisting quantum phases emerge under these conditions. Case ② [see Fig. 3(b)]: A similar examination can be conducted on expression (6). The results indicate that while the ME $E_c = \frac{1}{\lambda} + \sqrt{\frac{1}{\lambda^2} + \frac{2t}{\lambda}} + 2$ and the MME $E_c = \lambda - t$ remain unchanged, the ME $E_c = -\frac{1}{\lambda} - \sqrt{\frac{1}{\lambda^2} - \frac{2t}{\lambda}} + 2$ and the MME $E = -\lambda - t$ merge into one point: $E_c = -2$. Thus, only a three-state coexisting quantum phase emerges under these circumstances. Case ③ [see Fig. 3(c)]: In this case, only two MMEs ($E_c = \pm 2$) are possible, leading to a two-state (Localized + Multifractal) coexisting quantum phase. This occurs because the ME $E_c = \frac{1}{\lambda} + \sqrt{\frac{1}{\lambda^2} + \frac{2t}{\lambda}} + 2$ and the MME $E_c = \lambda - t$ converge at $E_c = 2$.

Phases characterized with IPR.—We now analyze the IPR $\xi_{R(K)}$ of the eigenstates in lattice (or dual) spaces

$$\xi_{R(K)} = \sum_{n(k)=1}^N \sum_{s=a,b,c} |\psi_{n(k),s}|^4, \quad (7)$$

where $\psi_{n(k),s}$ denote the wave functions on sublattice $s = \{A, B, C\}$ within the n (k)-th primitive cell. The properties of the IPR are detailed in Table II. As the quasiperiodic intensity λ increases, a region exhibiting multifractal characteristics emerges from the flat band at $E = -t$. This observation supports the notion that multifractal states can arise from the flat band, ultimately leading to MMEs (see Fig. 2). It is noteworthy that the emergence of this multifractal region occurs exclusively when quasiperiodic modulation is applied to sublattices B or C , both of which are associated with the flat band. Furthermore, similar MMEs can also manifest in diamond flat-band lattices, as well as in cross-stitch and Lieb flat-band lattices, when subjected to partial quasiperiodic modulation [34].

Experimental realization on Rydberg atomic array.—The lattice model presented in Eq. (1) can be realized in various artificial quantum systems, for specificity, we consider a Rydberg atomic array to illustrate the experimental scheme. The Hamiltonian for the atomic array depicted in Fig. 1(c) can be expressed as

$$\begin{aligned} H_R = & \sum_n (J_{AB}\sigma_{n,A}^+\sigma_{n,B}^- + J_{AC}\sigma_{n,A}^+\sigma_{n,C}^- + J_{BC}\sigma_{n,B}^+\sigma_{n,C}^- \\ & + J_{AB}\sigma_{n,B}^+\sigma_{n+1,A}^- + J_{AC}\sigma_{n,C}^+\sigma_{n+1,A}^- + \text{H.c.}) \\ & + \frac{1}{2} \sum_n V_n(1 + \sigma_{n,C}^z), \end{aligned} \quad (8)$$

where $\sigma^\pm = \frac{1}{2}(\sigma_x \pm i\sigma_y)$. The dipole-dipole interaction between Rydberg atoms is given by $J_{ij} = \frac{d^2}{R_{ij}^3}(3\cos^2\theta_{ij} - 1)$, where d represents the transition dipole moment between the two Rydberg levels, R_{ij} (with $i, j = A, B, C$) is the distance between sites i and j , and θ_{ij} is the angle between R_{ij} and the quantization axis defined by the magnetic field \mathbf{B} [36–38]. J_{ii} can be effectively mitigated to zero by selecting the magic angle $\theta_{ii} = \theta_m = 54.7^\circ$. In SM [34], we demonstrate that the model in Eq. (8) is equivalent to the model presented in Eq. (1) under the conditions that $J_{AB} = J_{AC} = J$ and $J_{BC} = t$. To achieve identical coupling J_{ij} between sublattice A and sublattices B and C , the following conditions must hold: $R_1 = \frac{2R_y}{\sin\theta_A}$, $R_2 = \sqrt{R_1^2 + R_x^2 - 2R_1R_x\cos\theta_A}$, $R_3 = \sqrt{2R_1R_2\cos(\theta_1 + \theta_2)}$, where the angles $\theta_1 = \pi - \theta_m - \theta_A$, $\theta_2 = \theta_m - \arcsin\left(\frac{R_1}{R_2}\sin\theta_A\right)$, and $\theta_3 = \theta_m - \arcsin\left(\frac{2R_1}{R_3}\sin\theta_A\right)$. From these conditions, we can derive the coupling constants: $J = \frac{d^2}{R_1^3}(3\cos^2\theta_1 - 1) = \frac{d^2}{R_2^3}(3\cos^2\theta_2 - 1)$, and $t = \frac{d^2}{R_3^3}(3\cos^2\theta_3 - 1)$.

The LEs and IPRs can be determined through the measurement of a quantity, denoted as $P_{\alpha,n}$, which is defined subsequently. The dynamics of the system governed by the Hamiltonian H_R satisfy the Schrödinger equation: $|\psi(t)\rangle = e^{-iH_R t}|\psi(0)\rangle = \sum_\alpha C_\alpha e^{-iE_\alpha t}|\psi_\alpha\rangle$, where $\alpha \in \{1, 2, 3, \dots, N\}$ corresponds to the eigenvalue index. The initial state is selected as $|\psi(0)\rangle_n = |0\rangle_1 \cdots |0\rangle_{n-1} \left(\frac{|0\rangle_n + |1\rangle_n}{\sqrt{2}}\right) |0\rangle_{n+1} \cdots |0\rangle_N$. During the evolution process, one can measure the time evolution curve of $\langle\sigma_n^+\rangle = \langle\sigma_n^x\rangle + i\langle\sigma_n^y\rangle$, and subsequently apply a Fourier transform to obtain the squared modulus of the transformation for various frequencies α , denoted as $P_{\alpha,n}$ [34, 39]. Upon the derivation of $P_{\alpha,n}$, the corresponding IPR ξ can be directly derived using the equation:

$$\xi_R(E_\alpha) = \sum_n P_{\alpha,n}^2. \quad (9)$$

Fig. 4 illustrates the IPR results for a system composed of six primitive cells. Furthermore, the wave function of a localized state can be expressed as

$$\psi_{R/K} \propto \max\{P_{\alpha,n}\} e^{-\gamma_{R/K}(n-n_0)}, \quad (10)$$

where $\max\{P_{\alpha,n}\}$ represents the maximum amplitude at a fixed α , and n_0 corresponds to the site with the maximum amplitude. By selecting three parameter points (triangle, star, square) in different phase regions depicted in Fig. 4(a,b), one can obtain the values for $\gamma_{R/K}$, as shown in Fig. 4(c-f), for wave functions characterized as extended, multifractal, and localized states, respectively. The results presented in Fig. 4 indicate that six primitive cells are sufficient to capture the principal phenomena predicted in this study. Notably, recent advancements in laboratory settings have successfully enabled the control of several hundred Rydberg atoms [42].

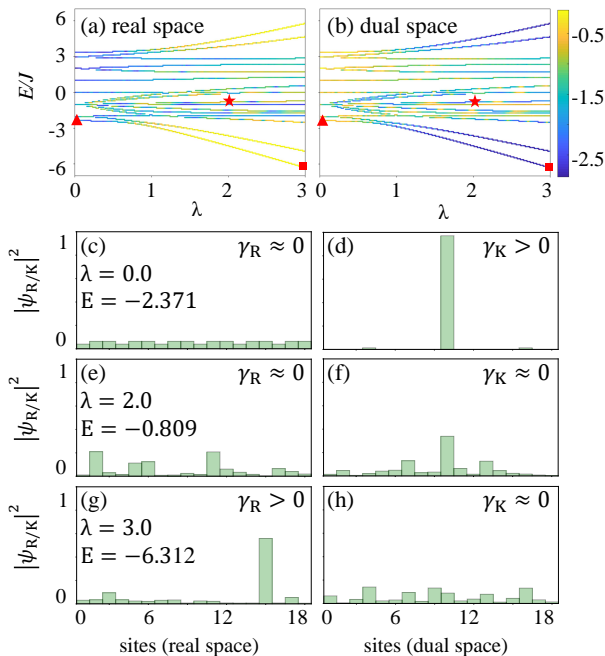


FIG. 4. (a,b) The IPRs and (c-h) LEs for 6 unit cells.

Conclusion.—We have introduced a class of one-dimensional, exactly solvable lattice models that exhibit a complete set of MMEs and multiple-state coexisting quantum phases. These phases can be characterized by the LEs and IPRs. Moreover, these models can be readily realized in artificial quantum systems, such as Rydberg atomic arrays and superconducting circuits. We have demonstrated that the LEs and IPRs can be measured using a spectroscopy measurement approach.

Acknowledgements.—We thank Chang Li and Yan-Xiong Du for their insightful suggestions, Ling-Feng Yu and Rui-Jie Chen for their programming and computing support. This work was supported by the National Key Research and Development Program of China (Grant No.2022YFA1405300), the National Natural Science Foundation of China (Grant No.12074180), Innovation Program for Quantum Science and Technology (Grant No. 2021ZD0301700), the Guangdong Basic and Applied Basic Research Foundation (Grants No.2021A1515012350), and Guangdong Provincial Quantum Science Strategic Initiative(GDZX2304002).

* Corresponding author: slzhu@scnu.edu.cn

† Corresponding author: lizphys@m.scnu.edu.cn

- [1] P. W. Anderson, Absence of diffusion in certain random lattices, *Phys. Rev.* **109**, 1492 (1958).
 [2] S. Aubry and G. André, Analyticity breaking and Anderson localization in incommensurate lattices, *Ann. Israel*

- Phys. Soc* **3**, 18 (1980).
 [3] N. F. Mott, Electrons in disordered structures, *Adv. Phys.* **50**, 865 (1967).
 [4] F. Liu, S. Ghosh, and Y. D. Chong, Localization and adiabatic pumping in a generalized Aubry-André-Harper model, *Phys. Rev. B* **91**, 014108 (2015).
 [5] J. Wang, X.-J. Liu, X. Gao, and H. Hu, Phase diagram of a non-Abelian Aubry-André-Harper model with p-wave superfluidity, *Phys. Rev. B* **93**, 104504 (2016).
 [6] T. Geisel, R. Ketzmerick, and G. Petschel, New Class of Level Statistics in Quantum Systems with Unbounded Diffusion, *Phys. Rev. Lett.* **66**, 1651 (1991).
 [7] S. Y. Jitomirskaya, Metal-insulator transition for the almost Mathieu operator, *Ann. Math.* **150**, 1159 (1999).
 [8] T. C. Halsey, M. H. Jensen, L. P. Kadanoff, I. Procaccia, and B. I. Shraiman, Fractal measures and their singularities: The characterization of strange sets, *Phys. Rev. A* **33**, 1141 (1986).
 [9] A. D. Mirlin, Y. V. Fyodorov, A. Mildenberger, and F. Evers, Exact Relations between Multifractal Exponents at the Anderson Transition, *Phys. Rev. Lett.* **97**, 046803 (2006).
 [10] H. Hiramoto and S. Abe, Dynamics of an electron in quasicrystalline systems. II. Harper's model, *J. Phys. Soc. Jpn.* **57**, 1365 (1988).
 [11] R. Ketzmerick, K. Kruse, S. Kraut, and T. Geisel, What Determines the Spreading of a Wave Packet? *Phys. Rev. Lett.* **79**, 1959 (1997).
 [12] J. Mayoh and A.M. García-García, Global critical temperature in disordered superconductors with weak multifractality, *Phys. Rev. B* **92**, 174526 (2015).
 [13] M.V. Feigel'man, L. B. Ioffe, V. E. Kravtsov, and E. A. Yuzbashyan, Eigenfunction Fractality and Pseudogap State near the Superconductor-Insulator Transition, *Phys. Rev. Lett.* **98**, 027001 (2007).
 [14] M.V. Feigel'man, L. B. Ioffe, V. E. Kravtsov, and E. Cuevas, Fractal superconductivity near localization threshold, *Ann. Phys(NY)*. **325**, 1390 (2010).
 [15] Z. Fan, G.-W. Chern and S.-Z. Lin, Enhanced superconductivity in quasicrystalline crystals, *Phys. Rev. Res.* **3**, 023195 (2021).
 [16] X. Zhang and M. S. Foster, Enhanced amplitude for superconductivity due to spectrum-wide wave function criticality in quasicrystalline and power-law random hopping-models, *Phys. Rev. B* **106**, L180503 (2022).
 [17] X. Deng, S. Ray, S. Sinha, G. V. Shlyapnikov, and L. Santos, One-Dimensional Quasicrystals with Power-Law Hopping, *Phys. Rev. Lett.* **123**, 025301 (2019).
 [18] Y. Wang, L. Zhang, W. Sun, T.-F. J. Poon, and X.-J. Liu, Quantum phase with coexisting localized, extended, and critical zones, *Phys. Rev. B* **106**, L140203 (2022).
 [19] Y. Wang, Mobility edges and critical regions in a periodically kicked incommensurate optical Raman lattice, *Phys. Rev. A* **106**, 053312 (2022).
 [20] X. Lin, X. Chen, G.-C. Guo, and M. Gong, General approach to the critical phase with coupled quasicrystalline chains, *Phys. Rev. B* **108**, 174206 (2023).
 [21] S.-Z. Li and Z. Li, Emergent recurrent extension phase transition in a quasicrystalline chain, arXiv:2304.11811.
 [22] R. Qi, J. Cao, and X.-P. Jiang, Multiple localization transitions and novel quantum phases induced by a staggered on-site potential, *Phys. Rev. B* **107**, 224201 (2023).
 [23] Q. Dai, Z. Lu, and Z. Xu, Emergence of multifractality through cascadelike transitions in a mosaic interpolating

- Aubry-André-Fibonacci chain, *Phys. Rev. B* **108**, 144207 (2023).
- [24] C. Guo, Multiple intermediate phases in the interpolating Aubry-André-Fibonacci model, *Phys. Rev. B* **109**, 174203 (2024).
- [25] T. Liu, X. Xia, S. Longhi, and L. Sanchez-Palencia, Anomalous mobility edges in one-dimensional quasiperiodic models, *SciPost Phys.* **12**, 27 (2022).
- [26] Y.-C. Zhang and Y.-Y. Zhang, Lyapunov exponent, mobility edges, and critical region in the generalized Aubry-André model with an unbounded quasiperiodic potential, *Phys. Rev. B* **105**, 174206 (2022).
- [27] Z. Wang, Y. Zhang, L. Wang, and S. Chen, Engineering mobility in quasiperiodic lattices with exact mobility edges, *Phys. Rev. B* **108**, 174202 (2023).
- [28] T. Liu, and X. Xu, Predicted Critical State Based on Invariance of the Lyapunov Exponent in Dual Spaces, *Chin. Phys. Lett.* **41** 017102 (2024).
- [29] X.-C. Zhou, Y. Wang, T.-F. J. Poon, Q. Zhou, and X.-L. Liu, Exact new mobility edges between critical and localized states, *Phys. Rev. Lett.* **131**, 176401 (2023).
- [30] B. Simon and T. Spencer, Trace class perturbations and the absence of absolutely continuous spectra, *Commun. Math. Phys.* **125**, 113 (1989).
- [31] M. Gonçalves, B. Amorim, E. Castro, and P. Ribeiro, Critical Phase Dualities in 1D Exactly Solvable Quasiperiodic Models, *Phys. Rev. Lett.* **131**, 186303 (2023).
- [32] M. Gonçalves, B. Amorim, E. V. Castro, and P. Ribeiro, Renormalization-group theory of 1D quasiperiodic lattice models with commensurate approximants, *Phys. Rev. B* **108**, L100201 (2023);
- [33] A. Avila, Global theory of one-frequency Schrödinger operators, *Acta. Math.* **1**, 215 (2015).
- [34] See Supplemental Material for details of the case of "flat band irrelative" quasiperiodic modulation (I) and the Lyapunov exponents (II). (III) provides the process from analytical expressions to phase diagram. (IV) exhibits the corresponding critical exponents. (V) More evidence to support the universality of the theory. (VI) Experimental scheme. The SM includes Ref. [26, 28, 33, 35, 36, 39–48].
- [35] C. Danieli, J. D. Bodyfelt, and S. Flach, Flat-band engineering of mobility edges, *Phys. Rev. B* **91**, 235134 (2015).
- [36] S. de Léséleuc, V. Lienhard, P. Scholl, D. Barredo, S. Weber, N. Lang, H. P. Büchler, T. Lahaye, and A. Browaeys, Observation of a symmetry-protected topological phase of interacting bosons with Rydberg atoms, *Science* **365**, 775 (2019).
- [37] V. Lienhard, P. Scholl, S. Weber, D. Barredo, S. de Léséleuc, R. Bai, N. Lang, M. Fleischhauer, H. P. Büchler, T. Lahaye, and A. Browaeys, Realization of a density-dependent perierls phase in a synthetic, spin-orbit coupled Rydberg system, *Phys. Rev. X* **10**, 021031 (2020).
- [38] A. Browaeys and T. Lahaye, Many-body physics with individually controlled Rydberg atoms, *Nat. Phys.* **16**, 132 (2020).
- [39] P. Roushan, C. Neill, J. Tangpanitanon, V. M. Bastidas, A. Megrant, R. Barends, Y. Chen, Z. Chen, B. Chiaro, A. Dunsworth, A. Fowler, B. Foxen, M. Giustina, E. Jeffrey, J. Kelly, E. Lucero, J. Mutus, M. Neeley, C. Quintana, D. Sank, A. Vainsencher, J. Wenner, T. White, H. Neven, D. G. Angelakis, J. Martinis, Spectroscopic signatures of localization with interacting photons in superconducting qubits, *Science* **358**, 1175 (2017).
- [40] S. Longhi, Metal-insulator phase transition in a non-Hermitian Aubry-André-Harper model, *Phys. Rev. B* **100**, 125157 (2019).
- [41] F. Evers and A. D. Mirlin, Anderson transitions, *Rev. Mod. Phys.* **80**, 1355 (2008).
- [42] S. Ebadi, T. T. Wang, H. Levine, A. Keesling, G. Semeghini, A. Omran, D. Bluvstein, R. Samajdar, H. Pichler, W. W. Ho, S. Choi, S. Sachdev, M. Greiner, V. Vuletić, and M. D. Lukin, Quantum phases of matter on a 256-atom programmable quantum simulator, *Nature (London)* **595**, 227 (2021).
- [43] T. Manovitz, S. H. Li, S. Ebadi, R. Samajdar, A. A. Geim, S. J. Evered, D. Bluvstein, H. Zhou, N. U. Köyliüoğlu, J. Feldmeier, P. E. Dolgirev, N. Maskara, M. Kalinowski, S. Sachdev, D. A. Huse, M. Greiner, V. Vuletić, M. D. Lukin, Quantum coarsening and collective dynamics on a programmable quantum simulator, *arXiv:2407.03249*.
- [44] E. H. Lieb, Two Theorems on the Hubbard Model, *Phys. Rev. Lett.* **62**, 1201 (1989).
- [45] G. Bornet, G. Emperauger, C. Chen, B. Ye, M. Block, M. Bintz, J. A. Boyd, D. Barredo, T. Comparin, F. Mezzacapo, T. Roscilde, T. Lahaye, N. Y. Yao and A. Browaeys, Scalable spin squeezing in a dipolar Rydberg atom array, *Nature (London)* **621**, 728 (2023).
- [46] D. Bluvstein, S. J. Evered, A. A. Geim, S. H. Li, H. Zhou, T. Manovitz, S. Ebadi, M. Cain, M. Kalinowski, D. Hangleiter, J. P. B. Ataiades, N. Maskara, I. Cong, X. Gao, P. S. Rodriguez, T. Karolyshyn, G. Semeghini, M. J. Gullans, M. Greiner, V. Vuletić, and M. D. Lukin, Logical quantum processor based on reconfigurable atom arrays, *Nature (London)* **626**, 58 (2024).
- [47] S.-A. Guo, Y.-K. Wu, J. Ye, L. Zhang, W.-Q. Lian, R. Yao, Y. Wang, R.-Y. Yan, Y.-J. Yi, Y.-L. Xu, B.-W. Li, Y.-H. Hou, Y.-Z. Xu, W.-X. Guo, C. Zhang, B.-X. Qi, Z.-C. Zhou, L. He and L.-M. Duan, A site-resolved two-dimensional quantum simulator with hundreds of trapped ions, *Nature (London)* **630**, 613 (2024).
- [48] IBM Quantum, and Community. Qiskit: An open-source framework for quantum computing (2021).

**Supplementary materials for:
Multifractal-enriched mobility edges and emergent quantum phases
in one-dimensional exactly solvable lattice models**

CONTENTS

References	5
I. Quasiperiodic modulation on the "flat band irrelative" sublattice	7
II. Derivation of Lyapunov exponents	8
II-1. Real space	9
II-2. Dual space	10
III. From analytical expressions to phase diagram	11
III-1. The case of $t < 2$	12
III-2. The case of $t \geq 2$	13
IV. The corresponding critical exponents	14
V. More evidence to support the universality of the theory	15
V-1. Quasiperiodic cross-stitch lattice	15
A. The LE of lattice space	15
B. The LE of dual space	17
C. Mobility edge	18
V-2. Quasiperiodic Lieb lattice	19
A. The LE of lattice space	20
B. The LE of dual space	21
C. Mobility edge	22
VI. Experimental scheme of the programmable Rydberg atomic array	23
VII. The measurement scheme	25
VII-1. Basic principles	25
VII-2. Experimental measurements of the IPRs	27
VII-3. Experimental measurements of the LEs	27

I. QUASIPERIODIC MODULATION ON THE "FLAT BAND IRRELATIVE" SUBLATTICE

The Hamiltonian of the diamond structure lattice with quasiperiodic potential on the sublattice A reads

$$H_R = \sum_{n=1}^N (J a_n^\dagger b_n + J a_n^\dagger c_n + t b_n^\dagger c_n + \text{H.c.}) + \sum_{n=1}^{N-1} (J b_n^\dagger a_{n+1} + J c_n^\dagger a_{n+1} + \text{H.c.}) + \sum_{n=1}^N V_{a,n} a_n^\dagger a_n, \quad (\text{S1})$$

and the corresponding eigenequations are

$$\begin{aligned} \psi_{b,n-1} + \psi_{c,n-1} + \psi_{b,n} + \psi_{c,n} + V_n \psi_{a,n} &= E \psi_{a,n}, \\ \psi_{a,n+1} + \psi_{a,n} + t \psi_{c,n} &= E \psi_{b,n}, \\ \psi_{a,n+1} + \psi_{a,n} + t \psi_{b,n} &= E \psi_{c,n}. \end{aligned} \quad (\text{S2})$$

Comparing the equations in the second and third rows, one can get $\psi_{b,n} = \psi_{c,n}$. Substituting it into the equation in the first row, we obtain recursion formula about ψ_a

$$\psi_{a,n+1} + \frac{E-t}{2} V_n \psi_{a,n} + \psi_{a,n-1} = \frac{E^2 - Et - 4}{2} \psi_{a,n}. \quad (\text{S3})$$

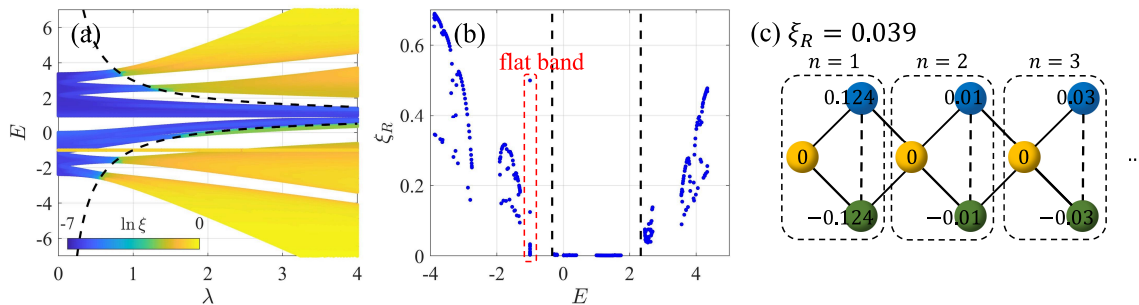


FIG. S1. (a) The IPR ξ_R versus λ , where the black dashed line is the mobility edge (ME) E_c . (b) The IPR ξ_R versus E for $\lambda = 1.5$, where the black dashed line is the ME $E_c = \pm \frac{4}{3} + 1$. (c) Amplitudes of the flat-band $E = -t$ eigenstates with IPR $\xi_R = 0.039$ in the first three primitive cells at $\lambda = 1.5$. Throughout, $N = 377$ and $t = 1$.

Under the condition of $V = \frac{\lambda(E-t)}{2}$ and $E' = \frac{E^2 - Et}{2} - 2$, the result of the eigenequation is consistent with the traditional AA model, so the ME in the system can be determined by the following equation of the critical energy, i.e.,

$$\left| \frac{\lambda(E_c - t)}{2} \right| = 1. \quad (\text{S4})$$

Thus, we can obtain the MMEs's analytical expressions as

$$E_c = \pm \frac{2}{\lambda} + t. \quad (\text{S5})$$

The results given by the analytic expression as well as that by the numerical IPR are both plotted in Fig. S1(a). The results reveal that, under such circumstances, there emerges no multifractal region in the system, which means the ME E_c only separates the extended states from the localized states.

Besides, we find that the flat band at $E = -t$ is not destroyed as the quasiperiodic strength increases, which is significantly different from the case where the quasiperiodic modulation is exerted at the "flat band related" sublattice. As an example, we fix the parameter $\lambda = 1.5$, and show the corresponding IPR values of all eigenstates of the system with different E in Fig. S1(b). The results demonstrate that there are still quite a number of eigenstates in the system at the flat band $E = -t$, which is evidence that this quasiperiodic modulation cannot destroy the flat band.

Moreover, in Fig. S1(c), we show the amplitude distribution of the wave function for a specific eigenstate ($\xi_R = 0.039$, $\lambda = 1.5$) at the flat band energy. As in the case absent of quasiperiodic modulation ($\lambda = 0$), all eigenstates corresponding to the flat band are the compact localized states [35], i.e., states with the structure of $\psi_n = (0, 1, -1)^T \delta_{n, n_0} / \sqrt{2}$, which will only appear in the B and C sublattice but not the A sublattice. This again shows that MMEs can only be induced if quasiperiodic modulation is exerted on the "flat band related" sublattice.

II. DERIVATION OF LYAPUNOV EXPONENTS

In the main text, we briefly introduce the LE in the lattice and dual spaces. Now, we exhibit a more detailed derivation process of LEs by means of Avila's global theory [33]. The definition of the LE is

$$\gamma_{R(K)} = \lim_{N \rightarrow \infty} \frac{1}{N} \ln \left\| \prod_{n(k)=1}^N T_{n(k)} \right\|, \quad (\text{S6})$$

where $\|\cdot\|$ denotes the matrix norm. $T_{n(k)}$ represents the transfer matrix and $\gamma_{R(K)}$ corresponds to the LE of the eigenstate corresponding to the eigenvalue E in lattice (dual) space. For localized (extended) eigenstates in lattice space, $\gamma_R > 0$ and $\gamma_K = 0$ ($\gamma_R = 0$ and $\gamma_K > 0$). For multifractal states, the wave function is delocalized in both spaces, so the LE satisfies $\gamma_R = \gamma_K = 0$ [28].

II-1. Real space

Here, we give a specific derivation of the real space LE. The Hamiltonian quantity of the real space is written as

$$H_R = \sum_{n=1}^N (Ja_n^\dagger b_n + Ja_n^\dagger c_n + tb_n^\dagger c_n + \text{H.c.}) + \sum_{n=1}^{N-1} (Jb_n^\dagger a_{n+1} + Jc_n^\dagger a_{n+1} + \text{H.c.}) + \sum_{n=1}^N V_n c_n^\dagger c_n, \quad (\text{S7})$$

and the corresponding eigenequation as

$$\psi_{c,n+1} = \frac{E^3 - (E^2 - 2)V_n - t^2 E - 4(E+t)}{2(E+t) - V_{n+1}} \psi_{c,n} - \frac{2(E+t) - V_{n-1}}{2(E+t) - V_{n+1}} \psi_{c,n-1}. \quad (\text{S8})$$

By extracting coefficients, one can obtain the corresponding transfer matrix as

$$T_n = A_n B_n, \quad (\text{S9})$$

where

$$\begin{aligned} A_n &= 1/M_{n+1} \\ B_n &= \begin{bmatrix} E^3 - (E^2 - 2)V_n - t^2 E - 4(E+t) & -M_{n-1} \\ M_{n+1} & 0 \end{bmatrix} \end{aligned} \quad (\text{S10})$$

with $M_n = 2(E+t) - V_n$. According to the above expression, the LE can be divided into two parts, that is, $\gamma_R = \gamma_A + \gamma_B$, in which [40]

$$\gamma_A = \lim_{N \rightarrow \infty} \frac{1}{N} \ln \prod_{n=1}^N \frac{1}{|2(E+t) - 2\lambda \cos(2\pi\alpha n + \theta)|} = \begin{cases} \ln \left| \frac{1}{|E+t| + \sqrt{(E+t)^2 - \lambda^2}} \right|, & |E+t| > \lambda, \\ \ln \left| \frac{1}{\lambda} \right|, & |E+t| \leq \lambda. \end{cases} \quad (\text{S11})$$

For γ_B , we apply Avila's global theory of one-frequency analytical $SL(2, \mathbb{R})$ cocycle [33]. The first step is to perform an analytical continuation of the global phase $\theta \rightarrow \theta + i\epsilon$ in B_n . In large ϵ limit, one can get

$$B_n = e^{-i2\pi\alpha n + \theta} e^\epsilon \begin{pmatrix} -\lambda E^2 - 2\lambda & \lambda e^{i2\pi\alpha} \\ -\lambda e^{-i2\pi\alpha} & 0 \end{pmatrix} + \mathcal{O}(1). \quad (\text{S12})$$

According to Avila's global theory, γ_B , as a function of ϵ , is a convex piecewise linear function with integer slopes [33]. The discontinuity of the slope occurs when E belongs to the spectrum of Hamiltonian (S7) except for $\gamma_B = 0$. Then, one can obtain

$$\gamma_B = \begin{cases} \ln \left| \lambda \frac{|E^2 - 2| + \sqrt{(E^2 - 2)^2 - 4}}{2} \right|, & |E^2 - 2| > 2, \\ \ln |\lambda|, & |E^2 - 2| \leq 2. \end{cases} \quad (\text{S13})$$

By combining γ_A (S11) and γ_B (S13), we obtain the LEs' analytical expressions with respect to the eigenvalue E in lattice space. Similarly, we can also get LEs' expressions in dual space. The complete LEs' expression in different energy region can be written as

$$\gamma_R = \begin{cases} \max \left\{ \ln \left| \frac{\lambda |E^2 - 2| + \lambda \sqrt{(E^2 - 2)^2 - 4}}{2|E+t| + 2\sqrt{(E+t)^2 - \lambda^2}} \right|, 0 \right\}, & |E+t| > \lambda \ \& \ |E^2 - 2| > 2, \\ \max \left\{ \ln \left| \frac{|E^2 - 2| + \sqrt{(E^2 - 2)^2 - 4}}{2} \right|, 0 \right\}, & |E+t| \leq \lambda \ \& \ |E^2 - 2| > 2, \\ \max \left\{ \ln \left| \frac{\lambda}{|t+E| + \sqrt{(t+E)^2 - \lambda}} \right|, 0 \right\}, & |E+t| > \lambda \ \& \ |E^2 - 2| \leq 2, \\ 0, & |E+t| \leq \lambda \ \& \ |E^2 - 2| \leq 2. \end{cases} \quad (\text{S14})$$

Since the logarithmic function in the second (third) row of the expression (S14) is always greater (smaller) than zero, $\gamma_R > 0$ ($\gamma_R = 0$) under the condition of $|E+t| \leq \lambda \ \& \ |E^2 - 2| > 2$ ($|E+t| > \lambda \ \& \ |E^2 - 2| \leq 2$). Then, one can

simplify the LE's expression as

$$\gamma_R = \begin{cases} \max \left\{ \ln \left| \frac{\lambda|E^2 - 2| + \lambda\sqrt{(E^2 - 2)^2 - 4}}{2|E + t| + 2\sqrt{(E + t)^2 - \lambda^2}} \right|, 0 \right\}, & |E + t| > \lambda \ \& \ |E^2 - 2| > 2, \\ \ln \left| \frac{|E^2 - 2| + \sqrt{(E^2 - 2)^2 - 4}}{2} \right|, & |E + t| \leq \lambda \ \& \ |E^2 - 2| > 2, \\ 0, & |E + t| > \lambda \ \& \ |E^2 - 2| \leq 2, \\ 0, & |E + t| \leq \lambda \ \& \ |E^2 - 2| \leq 2. \end{cases} \quad (\text{S15})$$

II-2. Dual space

The Hamiltonian in dual space can be read as

$$H_K = \sum_{k=1}^N (J_k a_k^\dagger b_k + J_k a_k^\dagger c_k + \text{H.c.}) + \sum_{n=1}^N (t b_n^\dagger c_n + \text{H.c.}) + \sum_{n=1}^{N-1} (\lambda c_{n+1}^\dagger c_n + \text{H.c.}). \quad (\text{S16})$$

Where $J_k = J + J e^{i(2\pi\alpha k)}$. Here, we insert a phase θ among J_k , i.e., $2\pi\alpha k \rightarrow (2\pi\alpha k + \theta)$, for the sake of the subsequent derivation of Avila's global theory. In fact, θ does not change the localization phase diagram, and in subsequent numerical calculations we set $\theta = 0$. From Hamiltonian (S16), one can obtain the corresponding eigenequation set, i.e.,

$$\begin{aligned} [1 + e^{i(2\pi\alpha k + \theta)}] \psi_{b,k} + [1 + e^{i(2\pi\alpha k + \theta)}] \psi_{c,k} &= E \psi_{a,k}, \\ [1 + e^{-i(2\pi\alpha k + \theta)}] \psi_{a,k} + t \psi_{c,k} &= E \psi_{b,k}, \\ \lambda \psi_{c,k+1} + \lambda \psi_{c,k-1} + [1 + e^{-i(2\pi\alpha k + \theta)}] \psi_{a,k} + t \psi_{b,k} &= E \psi_{c,k}. \end{aligned} \quad (\text{S17})$$

By combining the first and second rows of the above eigenequation set, we have

$$\psi_{a,k} = \frac{(t + E)[1 + e^{i(2\pi\alpha k + \theta)}]}{E^2 - 2 - 2 \cos(2\pi\alpha k + \theta)} \psi_{c,k}, \quad (\text{S18})$$

and

$$\psi_{b,k} = \frac{tE + 2 + 2 \cos(2\pi\alpha k + \theta)}{E^2 - 2 - 2 \cos(2\pi\alpha k + \theta)} \psi_{c,k}. \quad (\text{S19})$$

Then, one can obtain new eigenequation for the component ψ_c , i.e.,

$$\psi_{c,k+1} = -\frac{4t + 4E + t^2 E - E^3 - 4(t + E) \cos(2\pi\alpha k + \theta)}{\lambda[E^2 - 2 - 2 \cos(2\pi\alpha k + \theta)]} \psi_{c,k} - \psi_{c,k-1}. \quad (\text{S20})$$

Through the above equation, one can calculate the corresponding transfer matrix as

$$T_k = A_k B_k, \quad (\text{S21})$$

where

$$\begin{aligned} A_k &= \frac{1}{\lambda[E^2 - 2 - 2 \cos(2\pi\alpha k + \theta)]}, \\ B_k &= \begin{bmatrix} -4t - 4E - t^2 E + E^3 + 4(t + E) \cos(2\pi\alpha k + \theta) & -\lambda[E^2 - 2 - 2 \cos(2\pi\alpha k + \theta)] \\ \lambda[E^2 - 2 - 2 \cos(2\pi\alpha k + \theta)] & 0 \end{bmatrix}. \end{aligned} \quad (\text{S22})$$

The LE can be computed by $\gamma_K(E) = \gamma_A(E) + \gamma_B(E)$, in which [40]

$$\begin{aligned} \gamma_A &= \lim_{N \rightarrow \infty} \frac{1}{N} \ln \prod_{k=1}^N \frac{1}{\lambda[E^2 - 2 - 2 \cos(2\pi\alpha k + \theta)]} = \frac{1}{2\pi} \int_0^{2\pi} \ln \frac{1}{|\lambda[E^2 - 2 - 2 \cos(\phi)]|} d\phi \\ &= \begin{cases} \ln \left| \frac{2}{|\lambda E^2 - 2\lambda| + \sqrt{(\lambda E^2 - 2\lambda)^2 - 4\lambda^2}} \right|, & |E^2 - 2| > 2, \\ \ln \left| \frac{1}{\lambda} \right|, & |E^2 - 2| \leq 2. \end{cases} \end{aligned} \quad (\text{S23})$$

As for γ_B , one can use the Avila's global theory. The first step is to perform an analytical continuation of the global phase $\theta \rightarrow \theta + i\epsilon$ in B_k . In large ϵ limit, one can get

$$B_k = e^{-i2\pi\alpha k + \theta} e^\epsilon \begin{pmatrix} 2(t+E) & \lambda \\ -\lambda & 0 \end{pmatrix} + \mathcal{O}(1). \quad (\text{S24})$$

According to Avila's global theory, γ_B , as a function of ϵ , is a convex piecewise linear function with integer slopes [33]. One can obtain

$$\gamma_B = \begin{cases} \ln \left| 2|t+E| + 2\sqrt{(t+E)^2 - \lambda^2} \right|, & |E+t| > \lambda, \\ \ln |\lambda|, & |E+t| \leq \lambda. \end{cases} \quad (\text{S25})$$

By combining the information of γ_A and γ_B , one can obtain the corresponding LE versus E as

$$\gamma_K = \begin{cases} \max \left\{ \ln \left| \frac{2|E+t| + 2\sqrt{(E+t)^2 - \lambda^2}}{\lambda|E^2-2| + \lambda\sqrt{(E^2-2)^2 - 4}} \right|, 0 \right\}, & |E+t| > \lambda \ \& \ |E^2-2| > 2, \\ \max \left\{ \ln \left| \frac{2}{|E^2-2| + \sqrt{(E^2-2)^2 - 4}} \right|, 0 \right\}, & |E+t| \leq \lambda \ \& \ |E^2-2| > 2, \\ \max \left\{ \ln \left| \frac{|t+E| + \sqrt{(t+E)^2 - \lambda^2}}{\lambda} \right|, 0 \right\}, & |E+t| > \lambda \ \& \ |E^2-2| \leq 2, \\ 0, & |E+t| \leq \lambda \ \& \ |E^2-2| \leq 2. \end{cases} \quad (\text{S26})$$

Since the logarithmic function in the second row of the expression (S26) is always less than zero, $\gamma_K = 0$ under the condition of $|E+t| \leq \lambda$ & $|E^2-2| > 2$. Then, one can simplify the LE's expression as

$$\gamma_K = \begin{cases} \max \left\{ \ln \left| \frac{2|E+t| + 2\sqrt{(E+t)^2 - \lambda^2}}{\lambda|E^2-2| + \lambda\sqrt{(E^2-2)^2 - 4}} \right|, 0 \right\}, & |E+t| > \lambda \ \& \ |E^2-2| > 2, \\ 0, & |E+t| \leq \lambda \ \& \ |E^2-2| > 2, \\ \ln \left| \frac{|t+E| + \sqrt{(t+E)^2 - \lambda^2}}{\lambda} \right|, & |E+t| > \lambda \ \& \ |E^2-2| \leq 2, \\ 0, & |E+t| \leq \lambda \ \& \ |E^2-2| \leq 2. \end{cases} \quad (\text{S27})$$

The traditional ME is given by $\gamma_R = \gamma_K = 0$ for the first line of the Eq. (S15) and (S27), thus one can obtain four critical points on the energy axis, i.e.,

$$E_c = \begin{cases} \frac{1}{\lambda} + \sqrt{\frac{1}{\lambda^2} + \frac{2t}{\lambda} + 2}, \\ \frac{1}{\lambda} - \sqrt{\frac{1}{\lambda^2} + \frac{2t}{\lambda} + 2}, \\ -\frac{1}{\lambda} + \sqrt{\frac{1}{\lambda^2} - \frac{2t}{\lambda} + 2}, \\ -\frac{1}{\lambda} - \sqrt{\frac{1}{\lambda^2} - \frac{2t}{\lambda} + 2}. \end{cases} \quad (\text{S28})$$

Note that, E_c can only be in the energy region $|E+t| > \lambda$ & $|E^2-2| > 2$. Therefore, only two of the four critical points can be chosen, i.e., $E_{c,1} = \frac{1}{\lambda} + \sqrt{\frac{1}{\lambda^2} + \frac{2t}{\lambda} + 2}$ and $E_{c,2} = -\frac{1}{\lambda} - \sqrt{\frac{1}{\lambda^2} - \frac{2t}{\lambda} + 2}$. By considering the values of different parameters λ , one can directly obtain LEs in different cases.

III. FROM ANALYTICAL EXPRESSIONS TO PHASE DIAGRAM

For diamond lattice in the main text, the complete phase diagram consists of two parts, namely, the condition of $t < 2$ and $t \geq 2$. In this section, we will detail the complete process of obtaining phase diagram from analytic expression.

III-1. The case of $t < 2$

First, we discuss the case of $t < 2$. At present, we know that the LEs analytic expressions of lattice space and dual space are, respectively,

$$\gamma_R = \begin{cases} \gamma_{R,1}, & |E+t| > \lambda \ \& \ |E^2-2| > 2, \\ \gamma_{R,2}, & |E+t| \leq \lambda \ \& \ |E^2-2| > 2, \\ 0, & |E+t| > \lambda \ \& \ |E^2-2| \leq 2, \\ 0, & |E+t| \leq \lambda \ \& \ |E^2-2| \leq 2, \end{cases} \quad (\text{S29})$$

where $\gamma_{R,1} = \max \left\{ \ln \left| \lambda \frac{|E^2-2| + \sqrt{(E^2-2)^2-4}}{2|E+t| + 2\sqrt{(E+t)^2-\lambda^2}} \right|, 0 \right\}$, $\gamma_{R,2} = \ln \left| \frac{|E^2-2| + \sqrt{(E^2-2)^2-4}}{2} \right|$, and

$$\gamma_K = \begin{cases} \gamma_{K,1}, & |E+t| > \lambda \ \& \ |E^2-2| > 2, \\ 0, & |E+t| \leq \lambda \ \& \ |E^2-2| > 2, \\ \gamma_{K,2}, & |E+t| > \lambda \ \& \ |E^2-2| \leq 2, \\ 0, & |E+t| \leq \lambda \ \& \ |E^2-2| \leq 2, \end{cases} \quad (\text{S30})$$

where $\gamma_{K,1} = \max \left\{ \ln \left| \frac{2|E+t| + 2\sqrt{(E+t)^2-\lambda^2}}{\lambda|E^2-2| + \lambda\sqrt{(E^2-2)^2-4}} \right|, 0 \right\}$, $\gamma_{K,2} = \ln \left| \frac{|t+E| + \sqrt{(t+E)^2-\lambda}}{\lambda} \right|$.

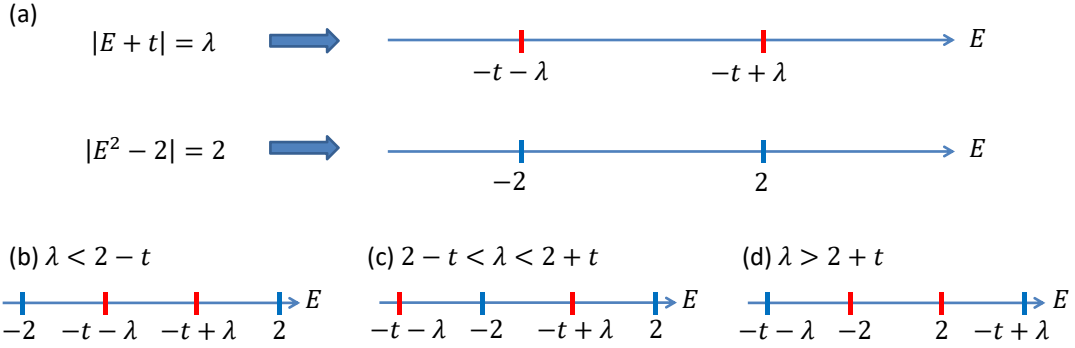


FIG. S2. (a) Four critical points on the energy axis. (b-d) Three possible relative positions of the four critical points.

From the equations (S29) and (S30), one can see that the values of LEs are determined by two inequalities no matter in the lattice space or in the dual space. Mathematically, since an inequality with an absolute value operation has two critical points, two inequalities will give four critical points [see Fig. S2]. Obviously, there are three different relationships of relative position between the four critical points, i.e.,

$$\begin{aligned} \textcircled{1} \quad & -2 < -t-\lambda < -t+\lambda < 2 \quad \text{for } \lambda \leq 2-t, \\ \textcircled{2} \quad & -t-\lambda < -2 < -t+\lambda < 2 \quad \text{for } 2-t \leq \lambda \leq 2+t, \\ \textcircled{3} \quad & -t-\lambda < -2 < 2 < -t+\lambda \quad \text{for } \lambda \geq 2+t. \end{aligned} \quad (\text{S31})$$

Furthermore, after determining the relative positions of the four critical points, one can obtain the values of LEs in different ranges on the energy axis through the information given by the inequalities. For example, let's consider the case of $\textcircled{1}$. We plot the process of getting the LEs' value on the energy axis in Fig. S3. As shown in the figure, we obtain that in the region of $E < -2$ or $E > 2$, the LE $\gamma_R = \gamma_{R,1}$. In other words, both $\gamma_R = \ln \left| \lambda \frac{|E^2-2| + \sqrt{(E^2-2)^2-4}}{2|E+t| + 2\sqrt{(E+t)^2-\lambda^2}} \right|$ and $\gamma_R = 0$ are true in this region. Then, we obtain $\gamma_R \geq 0$ in the region of $E < -2$ and $E > 2$ [see Fig. S3]. Perform the same analysis on the fourth line of the expression, we obtain $\gamma = 0$ in the region of $-t-\lambda < E < -t+\lambda$.

By analyzing the inequality information given by each line of the expression (S29) and (S30) step by step, one can obtain all LEs, which includes results both in the lattice and the dual spaces. By combining the above information from the two dual spaces, one can obtain the complete set of MMEs and all possible emergent quantum phases [see Fig. 3 in the main text].

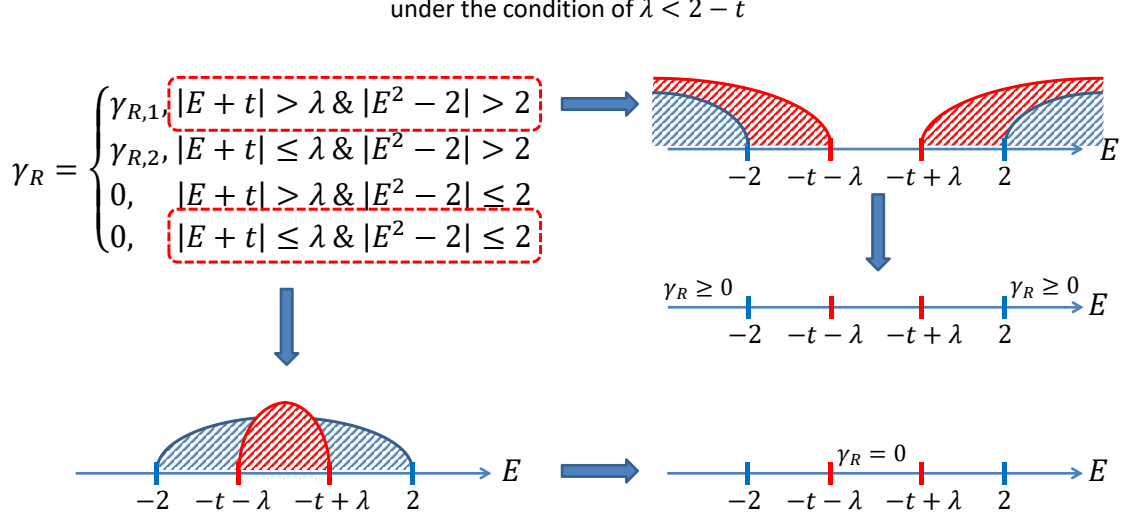


FIG. S3. The LEs for different regions determined by the analytical expressions.

III-2. The case of $t \geq 2$

Now, we turn to discuss the case of $t \geq 2$. The main analysis process is the same as previous subsection III-1. Under such circumstances, the critical points generated by the inequality also have three relative positions on the energy axis E , i.e.,

$$\begin{aligned} \textcircled{1} \quad & t - \lambda < -t + \lambda < -2 < 2 \quad \text{for } \lambda \leq t - 2, \\ \textcircled{2} \quad & t - \lambda < -2 < -t + \lambda < 2 \quad \text{for } t - 2 \leq \lambda \leq t + 2, \\ \textcircled{3} \quad & t - \lambda < -2 < 2 < -t + \lambda \quad \text{for } \lambda \geq t + 2. \end{aligned} \quad (\text{S32})$$

The complete phase diagram can be obtained using the same analysis method as in the previous Sec. II-1. We plot the phase diagram on energy axis E for different λ in Fig. S4(a-c). The results confirm again that all types of MMEs and multi-state coexisting quantum states emerge.

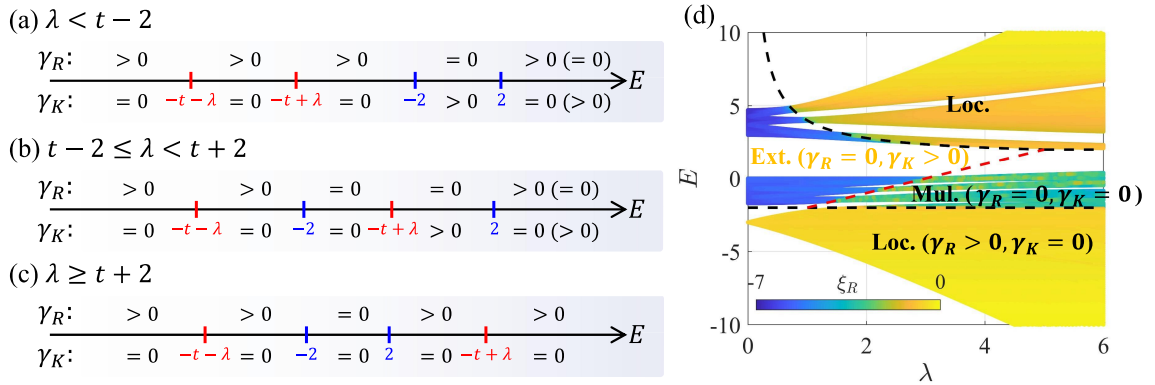


FIG. S4. LEs' Phase diagram versus E with different λ . (b) The lattice space IPR ξ_R versus λ , where the black (red) dashed line is the critical energy separating $\gamma_R > 0$ and $\gamma_R = 0$ regions ($\gamma_K > 0$ and $\gamma_K = 0$ regions) in lattice (dual) space. Throughout, $N = 377$ and $t = 1$.

Besides, the numerically calculated IPR is also shown in Fig. S4 to confirm the emergence of MMEs (in the region of $\lambda > t - 2$), which agrees perfectly with the theoretical expression (dashed lines). We summarize the results corresponding to the case of $t \geq 2$ in Tab. I.

TABLE I. MMEs and emergent quantum phases of flat-band partially-quasiperiodic diamond lattice for the case of $t \geq 2$.

Quasiperiodic strength	$\lambda < t - 2$		$t - 2 \leq \lambda < 2 + t$			$\lambda \geq t + 2$
Exact MMEs ($E_c =$)	$\frac{1}{\lambda} + \sqrt{\frac{1}{\lambda^2} + \frac{2t}{\lambda} + 2}$	-2	$\frac{1}{\lambda} + \sqrt{\frac{1}{\lambda^2} + \frac{2t}{\lambda} + 2}$	$\lambda - t$	-2	± 2
Separated states	Ext.* and Loc.	Ext. and Loc.	Ext. and Loc.	Ext. and Mul.	Ext. and Mul.	Loc. and Mul.
Possible phases	Ext.+Loc.		Ext.+Mul.+Loc.			Loc.+Mul.

*Ext.=Extended states; Loc.=Localized states; Mul.=Multifractal states.

IV. THE CORRESPONDING CRITICAL EXPONENTS

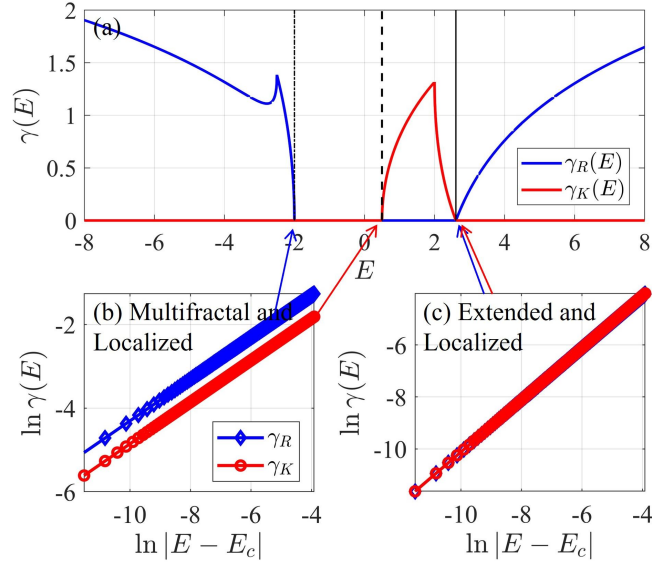


FIG. S5. (a) The LE versus E in the region of $E \in [-8, 8]$. $\ln \gamma$ versus $\ln |E - E_c|$ for the case of $E_c = -2$ and $E_c = 0.5$ (b), and the case of $E = 2.6103$ (c). The red and blue lines stand for the LEs in the lattice and dual spaces, respectively. Other parameters $t = 1$ and $\lambda = 1.5$.

Critical exponent, as an important indicator to discuss the universal class of phase transitions, has been widely used in the study of localized phase transitions. The standard Anderson phase transition from the extended phase to the localized phase corresponds to a critical exponent of $\mu = 1$ [41], while that of the phase transition from the multifractal phase to the localized phase is 0.5 [26].

Here we calculate the critical exponent of the model in the main text and plot that in Fig. S5.

First, we exhibit the LE in lattice and dual space for all eigenenergies between $E \in [-8, 8]$ at $\lambda = 1.5$ and $t = 1$ [see Fig. S5(a)]. It can be seen clearly that the LEs for ME separating the multifractal and localized states are very different from the LE for ME separating the extended and localized states. By fitting the LEs under log-log scale, we obtain the corresponding critical exponents, which equal to the slope of $\gamma_{R(K)}$ under log-log scale in Fig. S5(b)(c). On the one hand, from Fig. S5(b), one can find that the critical exponent $\nu = 1/2$ for the critical energy separating the multifractal and localized states ($E_c = -2$ for γ_R and $E_c = 0.5$ for γ_K). On the other hand, from Fig. S5(c), one can find that the corresponding critical exponent $\nu = 1$ for the critical energy separating the extended and localized states ($E_c = 2.6103$ for both γ_R and γ_K). The critical exponent again from another perspective supports the correctness of the results given by analyzing MMEs and IPR in the main text.

V. MORE EVIDENCE TO SUPPORT THE UNIVERSALITY OF THE THEORY

In order to prove the universality of the theory, we provide another two typical flat-band partially-quasiperiodic lattice models, namely, quasiperiodic cross-stitch lattice and quasiperiodic Lieb lattice.

V-1. Quasiperiodic cross-stitch lattice

First, we discuss MMEs and the emergent multi-state coexisting quantum phase in quasiperiodic cross-stitch lattice.

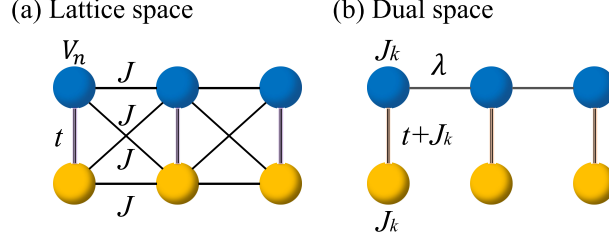


FIG. S6. The schematic diagram of the quasiperiodic cross-stitch lattice in lattice space (a) and in dual space (b). Blue and yellow balls correspond to sublattice A and B, respectively.

The geometric structure is shown schematically in Fig. S6(a) and the Hamiltonian can be written as

$$H_R = \sum_{n=1}^{N-1} J(a_n^\dagger b_{n+1} + a_n^\dagger a_{n+1} + b_n^\dagger a_{n+1} + b_n^\dagger b_{n+1} + \text{H.c.}) + \sum_{n=1}^N (ta_n^\dagger b_n + \text{H.c.}) + \sum_{n=1}^N V_n a_n^\dagger a_n, \quad (\text{S33})$$

where a_n (a_n^\dagger) and b_n (b_n^\dagger) represent the annihilation (creation) operators of sublattices A and B in the n -th primitive cell, respectively. J and t denote the inter- and intra-hopping strength, which are marked in the Fig. S6. N represents the total number of primitive cells. The quasiperiodic potential $V_n = 2\lambda \cos(2\pi\alpha n + \theta)$ is applied only on the sublattice A, where λ , α , and θ denote the quasiperiodic strength, an irrational number, and a phase offset, respectively. Under the condition of $\lambda = 0$, Hamiltonian (S33) will exhibit two bands with different dispersion relations. One is an exact flat-band of $E_k = -t$, the other is a dispersive band of $E_k = 4J \cos(k) + t$ [35].

By applying dual transform $a_n = \frac{1}{\sqrt{N}} \sum_k a_k e^{-i2\pi\alpha kn}$ and $b_n = \frac{1}{\sqrt{N}} \sum_k b_k e^{-i2\pi\alpha kn}$ for Hamiltonian (S33), one can get the Hamiltonian in dual space, which has a similar structure to a Fano defect quasiperiodic lattice [see Fig. S6(b)], i.e.,

$$H_K = \sum_{k=1}^{N-1} (\lambda a_k^\dagger a_{k+1} + \text{H.c.}) + \sum_{k=1}^N [(t + J_k) a_k^\dagger b_k + \text{H.c.}] + \sum_{k=1}^N J_k (a_k^\dagger a_k + b_k^\dagger b_k), \quad (\text{S34})$$

where $J_k = 2J \cos(2\pi\alpha k + \theta)$.

A. The LE of lattice space

The eigenequation for Hamiltonian (S33) is

$$\begin{aligned} \psi_{a,n-1} + \psi_{a,n+1} + \psi_{b,n-1} + \psi_{b,n+1} + t\psi_{b,n} &= (E - V_n)\psi_{a,n}, \\ \psi_{a,n-1} + \psi_{a,n+1} + \psi_{b,n-1} + \psi_{b,n+1} + t\psi_{a,n} &= E\psi_{b,n}. \end{aligned} \quad (\text{S35})$$

One can get the relationship between $\psi_{a,n}$ and $\psi_{b,n}$ as $\psi_{b,n} = (E + t - V_n)/(E + t)\psi_{a,n}$. Thus, from Eq. (S35), we obtain a new equation for the component $\psi_{a,n}$, i.e.,

$$\psi_{a,n+1} = \frac{E^2 - 2Et - t^2 - EV_n}{2(E + t) - V_{n+1}} \psi_{a,n} - \frac{2(E + t) - V_{n-1}}{2(E + t) - V_{n+1}} \psi_{a,n-1}, \quad (\text{S36})$$

from which we directly obtain the corresponding transfer matrix

$$T_n = A_n B_n, \quad (\text{S37})$$

where

$$A_n = \frac{1}{2(E+t) - V_{n+1}}, \quad B_n = \begin{pmatrix} E^2 - 2Et - t^2 - EV_n & -2(E+t) + V_{n-1} \\ 2(E+t) - V_{n+1} & 0 \end{pmatrix}. \quad (\text{S38})$$

The LE can be written as $\gamma_R = \gamma_A + \gamma_B$, in which

$$\begin{aligned} \gamma_A &= \lim_{N \rightarrow \infty} \frac{1}{N} \ln \prod_{n=1}^N \frac{1}{|2(E+t) - 2\lambda \cos[2\pi\alpha(n+1) + \theta]|} \\ &= \frac{1}{2\pi} \int_0^{2\pi} \ln \frac{1}{|2(E+t) + 2\lambda \cos(\phi)|} d\phi \\ &= \begin{cases} \ln \left| \frac{1}{|E+t| + \sqrt{(E+t)^2 - \lambda^2}} \right|, & |E+t| > \lambda, \\ \ln \left| \frac{1}{\lambda} \right|, & |E+t| \leq \lambda. \end{cases} \end{aligned} \quad (\text{S39})$$

As for γ_B , we apply Avila's global theory of one-frequency analytical $SL(2, \mathbb{R})$ cocycle [33]. The first step is to perform an analytical continuation of the global phase $\theta \rightarrow \theta + i\epsilon$ in B_n . In large ϵ limit, one can get

$$B_{n, \epsilon \rightarrow \infty} = e^{-i2\pi\alpha n + \theta} e^\epsilon \begin{pmatrix} -\lambda E & \lambda e^{i2\pi\alpha} \\ -\lambda e^{-i2\pi\alpha} & 0 \end{pmatrix} + \mathcal{O}(1), \quad (\text{S40})$$

According to Avila's global theory, as a function of ϵ , $\gamma_B(E)$ is a convex piecewise linear function with integer slopes [33]. The discontinuity of the slope occurs when E belongs to the spectrum of Hamiltonian H except for $\gamma_B(E) = 0$, which represents the extended states. We can get

$$\gamma_B(E) = \begin{cases} \ln \left| \frac{|\lambda E| + \sqrt{(\lambda E)^2 - 4\lambda^2}}{2} \right|, & |E| > 2, \\ \ln |\lambda|, & |E| \leq 2. \end{cases} \quad (\text{S41})$$

Combining the information of γ_A and γ_B , we obtain the LE γ_R versus E as

$$\gamma_R = \begin{cases} \max \left\{ \ln \left| \frac{|\lambda E| + \sqrt{(\lambda E)^2 - 4\lambda^2}}{|2(E+t)| + 2\sqrt{(E+t)^2 - \lambda^2}} \right|, 0 \right\}, & |E+t| > \lambda \ \& \ |E| > 2, \\ \max \left\{ \ln \left| \frac{|E| + \sqrt{E^2 - 4}}{2} \right|, 0 \right\}, & |E+t| \leq \lambda \ \& \ |E| > 2, \\ \max \left\{ \ln \left| \frac{\lambda}{|E+t| + \sqrt{(E+t)^2 - \lambda^2}} \right|, 0 \right\}, & |E+t| > \lambda \ \& \ |E| \leq 2, \\ 0, & |E+t| \leq \lambda \ \& \ |E| \leq 2. \end{cases} \quad (\text{S42})$$

Since the second (third) row of the LE expression satisfies $|E| > 2$ ($|E+t| < 2$), then $\gamma_R > 0$ ($\gamma_R = 0$). Finally, we can obtain the LE in the lattice space as

$$\gamma_R = \begin{cases} \max \left\{ \ln \left| \frac{|\lambda E| + \sqrt{(\lambda E)^2 - 4\lambda^2}}{|2(E+t)| + 2\sqrt{(E+t)^2 - \lambda^2}} \right|, 0 \right\}, & |E+t| > \lambda \ \& \ |E| > 2, \\ \ln \left| \frac{|E| + \sqrt{E^2 - 4}}{2} \right|, & |E+t| \leq \lambda \ \& \ |E| > 2, \\ 0, & |E+t| > \lambda \ \& \ |E| \leq 2, \\ 0, & |E+t| \leq \lambda \ \& \ |E| \leq 2. \end{cases} \quad (\text{S43})$$

B. The LE of dual space

The eigenequation of dual Hamiltonian (S34) is

$$\begin{aligned}\lambda(\psi_{a,k-1} + \psi_{a,k+1}) + J_k\psi_{a,k} + (t + J_k)\psi_{b,k} &= E\psi_{a,k}, \\ (t + J_k)\psi_{a,k} + J_k\psi_{b,k} &= E\psi_{b,k}.\end{aligned}\tag{S44}$$

Then, the corresponding transfer matrix in dual space is

$$T_k = A_k B_k,\tag{S45}$$

where

$$\begin{aligned}A_k &= \frac{1}{E - 2\cos(2\pi\alpha k + \theta)}, \\ B_k &= \begin{pmatrix} \frac{E^2 - 2(2E + t)\cos(2\pi\alpha k + \theta) - t^2}{E - 2\cos(2\pi\alpha k + \theta)} & -E + 2\cos(2\pi\alpha k + \theta) \\ \lambda & 0 \end{pmatrix}.\end{aligned}\tag{S46}$$

The LE can be written as $\gamma_R(E) = \gamma_A(E) + \gamma_B(E)$, in which

$$\begin{aligned}\gamma_A &= \lim_{N \rightarrow \infty} \frac{1}{N} \ln \prod_{k=1}^N \frac{1}{E - 2\cos(2\pi\alpha k + \theta)} = \frac{1}{2\pi} \int_0^{2\pi} \ln \frac{1}{|E + 2\cos(\phi)|} d\phi \\ &= \begin{cases} \ln \left| \frac{1}{|E| + \sqrt{(E)^2 - 4}} \right|, & |E + t| > \lambda, \\ 0, & |E + t| \leq \lambda. \end{cases}\end{aligned}\tag{S47}$$

As for γ_B , we apply Avila's global theory of one-frequency analytical $SL(2, \mathbb{R})$ cocycle [33]. The first step is to perform an analytical continuation of the global phase $\theta \rightarrow \theta + i\epsilon$ in B_k . In large ϵ limit, we can get

$$B_{k,\epsilon \rightarrow \infty} = e^{-i2\pi\alpha k + \theta} e^\epsilon \begin{pmatrix} -(2E + 2t) & 1 \\ -1 & 0 \end{pmatrix} + \mathcal{O}(1).\tag{S48}$$

According to Avila's global theory, as a function of ϵ , $\gamma_B(E)$ is a convex piecewise linear function with integer slopes [33]. The discontinuity of the slope occurs when E belongs to the spectrum of Hamiltonian H except for $\gamma_B(E) = 0$, which represents the extended states. One can obtain

$$\gamma_B = \begin{cases} \ln \left| \frac{|E + t| + \sqrt{(E + t)^2 - \lambda^2}}{\lambda} \right|, & |E + t| > \lambda, \\ 0, & |E + t| \leq \lambda. \end{cases}\tag{S49}$$

Combining with $\gamma_A(E)$, the LE for different E is

$$\gamma_K = \begin{cases} \max \left\{ \ln \left| \frac{2(E + t) + 2\sqrt{(E + t)^2 - \lambda^2}}{\lambda(E + \sqrt{E^2 - 4})} \right|, 0 \right\}, & |E + t| > \lambda \ \& \ |E| > 2, \\ \max \left\{ \ln \left| \frac{2}{|E| + \sqrt{E^2 - 4}} \right|, 0 \right\}, & |E + t| \leq \lambda \ \& \ |E| > 2, \\ \max \left\{ \ln \left| \frac{|E + t| + \sqrt{(E + t)^2 - \lambda^2}}{\lambda} \right|, 0 \right\}, & |E + t| > \lambda \ \& \ |E| \leq 2, \\ 0, & |E + t| \leq \lambda \ \& \ |E| \leq 2. \end{cases}\tag{S50}$$

Since the second (third) row of the LE satisfies $|E| > 2$ ($|E + t| < 2$), $\gamma_K = 0$ ($\gamma_K > 0$). Finally, we can obtain the LE of the lattice space as

$$\gamma_K = \begin{cases} \max \left\{ \ln \left| \frac{2(E + t) + 2\sqrt{(E + t)^2 - \lambda^2}}{\lambda(E + \sqrt{E^2 - 4})} \right|, 0 \right\}, & |E + t| > \lambda \ \& \ |E| > 2, \\ 0, & |E + t| \leq \lambda \ \& \ |E| > 2, \\ \ln \left| \frac{|E + t| + \sqrt{(E + t)^2 - \lambda^2}}{\lambda} \right|, & |E + t| > \lambda \ \& \ |E| \leq 2, \\ 0, & |E + t| \leq \lambda \ \& \ |E| \leq 2. \end{cases}\tag{S51}$$

C. Mobility edge

By comparing the expressions of γ_R and γ_K , one can find that in the region of $|E+t| \leq \lambda$ & $|E| \leq 2$, $\gamma_R = \gamma_K = 0$, indicating that the corresponding eigenstates in this region are multifractal critical states. For the rest of the energy region, the lattice and dual spaces have opposite localization properties, i.e., $\gamma_R = 0$ while $\gamma_K > 0$, or vice versa. Since the critical points satisfy a mirror-symmetric relationship between the case of $t < 0$ and the case of $t > 0$, here we will only exhibit the case of $t > 0$ as what we have done in the main text.

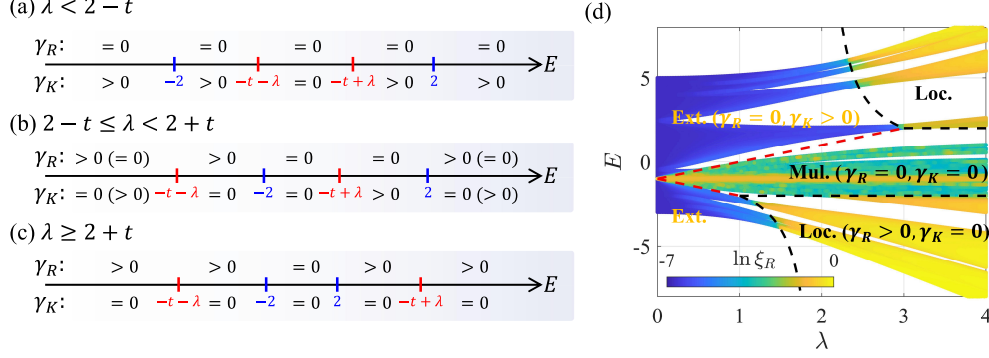


FIG. S7. (a-c) Phase diagram versus E with different λ for the case of $t < 2$. (d) The lattice space IPR ξ_R versus λ , where the black (red) dashed line is the critical energy separating $\gamma_R > 0$ and $\gamma_R = 0$ regions ($\gamma_K > 0$ and $\gamma_K = 0$ regions) in lattice (dual) space. The other parameters $N = 610$ and $t = 1$.

On the one hand, for the case of $t < 2$, from the inequalities in the analytic expressions (S43) and (S51), one can find that the cross-stitch model has the same four critical points as the diamond model in the main text, and they also divide the energy axis into five intervals. The difference is that $E_c = \frac{2t}{\lambda-2}$ is not within the energy interval $|E+t| > \lambda$ and $|E| > 2$ under the conditions of $\lambda < 2 - t$ and $\lambda \geq 2 + t$. That is to say, the three-state coexisting quantum phase can only emerge when $2 - t \leq \lambda < 2 + t$. In other words, since there is no localized (extended) state in the region of $\lambda < 2 - t$ ($\lambda \geq 2 + t$), only two-state coexisting quantum phases can emerge in certain circumstances [see Fig. S7(a-c)]. Furthermore, we numerically compute the corresponding IPR [see Fig. S7(d)]. The numerical results and analytical results show that MMEs and multi-state coexisting quantum phases will emerge in the system.

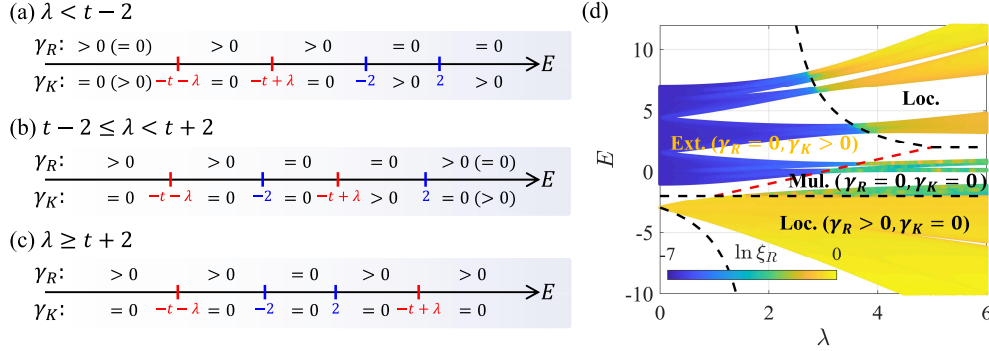


FIG. S8. (a-c) Phase diagram versus E with different λ for the case of $t \geq 2$. (d) The lattice space IPR ξ_R versus λ , where the black (red) dashed line is the critical energy separating $\gamma_R > 0$ and $\gamma_R = 0$ regions ($\gamma_K > 0$ and $\gamma_K = 0$ regions) in lattice (dual) space. The other parameters $N = 610$ and $t = 3$.

A similar analysis leads us to the phase diagram for $t \geq 2$, which is plotted in Fig. S8(a-c). The main difference between $t \leq 2$ and $t < 2$ is in the first stage of the phase diagram, i.e., the case of $\lambda < t - 2$. Under certain circumstances, the four critical points satisfy the relative position relation $-t - \lambda < -t + \lambda < -2 < 2$. By analyzing the interval given by the inequalities of the expressions (S43) and (S51), we find that it is impossible to have a region with multifractal states in this case. In other words, the system has only extended and localized states in this case. In the second stage ($2 - t < \lambda < 2 + t$), multi-state coexisting quantum phases emerge in the system and all types of MMEs are allowed [see Fig. S8(b)]. In the third stage ($\lambda \geq 2 + t$), the system has only MMEs separating the localized

state and the multifractal state [see Fig. S8(c)]. Furthermore, we provide the numerical IPR [see Fig. S8(d)], which is consistent with the conclusion given by the analytic expressions.

TABLE II. MMEs and quantum phases of partially-quasiperiodic cross-stitch lattice for the case of $t < 2$

Quasiperiodic strength	$\lambda < 2 - t$	$2 - t \leq \lambda < 2 + t$			$\lambda \geq 2 + t$
Exact MMEs ($E_c =$)	$\pm\lambda - t$	$\frac{2t}{\lambda-2}$	$\lambda - t$	-2	± 2
Separated states	Ext.* and Mul.	Ext. and Loc.	Ext. and Mul.	Loc. and Mul.	Loc. and Mul.
Possible phases	Ext.+Mul.	Ext.+Mul.+Loc.			Loc.+Mul.

*Ext.=Extended states; Loc.=Localized states; Mul.=Multifractal states.

TABLE III. MMEs and quantum phases of partially-quasiperiodic cross-stitch lattice for the case of $t \geq 2$

Quasiperiodic strength	$\lambda < t - 2$		$2 - t \leq \lambda < 2 + t$			$\lambda \geq 2 + t$
Exact MMEs ($E_c =$)	$\frac{2t}{\lambda-2}$	-2	$\frac{2t}{\lambda-2}$	$\lambda - t$	-2	± 2
Separated states	Ext.* and Loc.	Ext. and Loc.	Ext. and Loc.	Ext. and Mul.	Ext. and Mul.	Loc. and Mul.
Possible phases	Ext.+Loc.		Ext.+Mul.+Loc.			Loc.+Mul.

*Ext.=Extended states; Loc.=Localized states; Mul.=Multifractal states.

Finally, we summarize the MMEs and emergent quantum phases of the partially-quasiperiodic cross-stitch lattice in Tab. II and Tab. III. The results reveal that the system contains not only the traditional ME separating extended and localized states, but also the MMEs separating multifractal and localized states or separating multifractal and extended states. Meanwhile, exotic quantum phases featuring two-state coexistence (Ext. + Loc. or Loc. + Mul.) and three-state coexistence (Ext. + Mul. + Loc.) emerge.

This is another evidence supporting the conclusion: The MMEs and exotic quantum phases can emerge in the flat-band system.

V-2. Quasiperiodic Lieb lattice

Now, we will show another quasiperiodic flat-band model, i.e., the quasiperiodic Lieb lattice [44], and the schematic diagram is shown in Fig. S9(a). The corresponding Hamiltonian reads

$$H_R = \sum_{n=1}^N (ta_n^\dagger b_n + Jb_n^\dagger c_n + \text{H.c.}) + \sum_{n=1}^N (mb_{n+1}^\dagger c_n + \text{H.c.}) + \sum_{n=1}^N V_n a_n^\dagger a_n, \quad (\text{S52})$$

where $V_n = 2\lambda \cos(2\pi\alpha n + \theta)$. By means of the dual transform, we can obtain the Hamiltonian in dual space as

$$H_K = \sum_{k=1}^{N-1} \lambda (a_k^\dagger a_{k+1} + \text{H.c.}) + \sum_{k=1}^N [ta_k^\dagger b_k + (J + m_k)b_k^\dagger c_k + \text{H.c.}], \quad (\text{S53})$$

and the schematic diagram is shown in Fig. S9(b), where $m_k = me^{i(2\pi\alpha k + \theta)}$. When $\lambda = 0$, the Hamiltonian (S52) has a flat band $E = 0$. For the following discuss, we set $J = 1$ as the unit energy.

Note that, unlike the two flat-band models discussed earlier, the relative positions of the four critical points in this model are symmetric about the origin, so there are only two possibilities, namely $[-2, 2] \subseteq [-m-1, m+1]$, or $[-m-1, m+1] \subseteq [-2, 2]$. The obtained phase diagram is shown in Fig. S9(b). The corresponding IPR has also been given in Fig. S9(c).

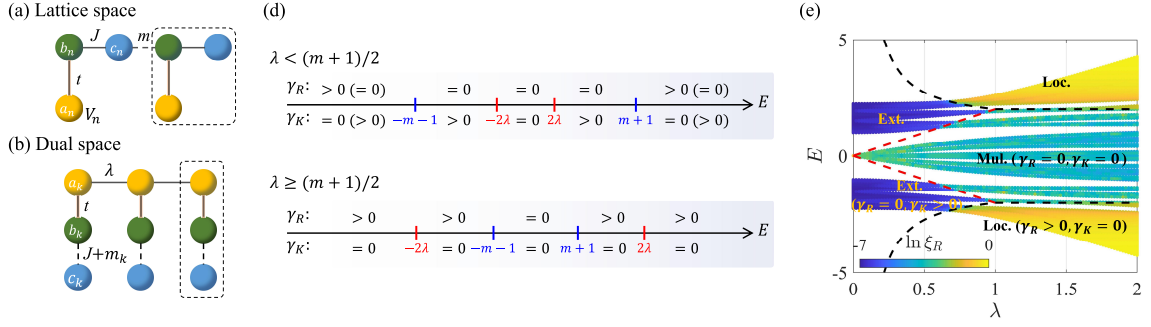


FIG. S9. (a) Lattice structure in real space and dual space. (b) The phase diagram of Lieb model. (c) IPR in lattice space ξ_R versus E for different λ , where the black (red) dashed line is the critical energy separating $\gamma_R(E) > 0$ ($\gamma_K(E) > 0$) and $\gamma_R(E) = 0$ ($\gamma_K(E) = 0$) in lattice (dual) space. In the computation, we set primitive cell number $N = 377$.

A. The LE of lattice space

The eigenequation for Hamiltonian (S52) is

$$\begin{aligned} V_n \psi_{a,n} + t \psi_{b,n} &= E \psi_{a,n}, \\ m \psi_{c,n-1} + t \psi_{a,n} + \psi_{c,n} &= E \psi_{b,n}, \\ \psi_{b,n} + m \psi_{b,n+1} &= E \psi_{c,n}. \end{aligned} \quad (\text{S54})$$

Then, one can simplify the Eq. (S54) into a component eigenequation with respect to ψ_c , i.e.,

$$\psi_{c,n+1} = \frac{(E^2 - m^2 - 1)(E - V_n) - Et^2}{m(E - V_n)} \psi_{c,n} - \psi_{c,n-1}. \quad (\text{S55})$$

Then, one can directly obtain the corresponding transfer matrix

$$T_n = A_n B_n, \quad (\text{S56})$$

where

$$\begin{aligned} A_n &= \frac{1}{m[E - 2\lambda \cos(2\pi\alpha n + \theta)]}, \\ B_n &= \begin{pmatrix} (E^2 - m^2 - 1)(E - V_n) - Et^2 & -m(E - V_n) \\ m(E - V_n) & 0 \end{pmatrix}. \end{aligned} \quad (\text{S57})$$

The LE can be written as $\gamma_R(E) = \gamma_A(E) + \gamma_B(E)$, in which

$$\begin{aligned} \gamma_A(E) &= \lim_{N \rightarrow \infty} \frac{1}{N} \ln \prod_{n=1}^N \frac{1}{m[E - 2\lambda \cos(2\pi\alpha n + \theta)]} \\ &= \begin{cases} \ln \left| \frac{2}{m(|E| + \sqrt{E^2 - 4\lambda^2})} \right|, & |E| > 2\lambda, \\ \ln \left| \frac{1}{m\lambda} \right|, & |E| \leq 2\lambda. \end{cases} \end{aligned} \quad (\text{S58})$$

For $\gamma_B(E)$, again, we apply Avila's global theory of one-frequency analytical $SL(2, \mathbb{R})$ cocycle [33]. The first step in the calculation is to perform an analytical continuation of the global phase $\theta \rightarrow \theta + i\epsilon$ in B_n . In large ϵ limit, one can obtain

$$B_{n,\epsilon \rightarrow \infty} = e^{-i2\pi\alpha n + \theta} e^\epsilon \begin{pmatrix} -\lambda(E^2 - m^2 - 1) & m\lambda \\ -m\lambda & 0 \end{pmatrix} + \mathcal{O}(1). \quad (\text{S59})$$

According to Avila's global theory, as a function of ϵ , $\gamma_B(E)$ is a convex piecewise linear function with integer slopes [33]. The discontinuity of the slope occurs when E belongs to the spectrum of Hamiltonian H except for

$\gamma_B(E) = 0$, which represents the extended states. Then, one can get

$$\gamma_B = \begin{cases} \ln \left| \lambda \frac{|E^2 - m^2 - 1| + \sqrt{(E^2 - m^2 - 1)^2 - 4m^2}}{2} \right|, & |E^2 - m^2 - 1| > 2m, \\ \ln |m\lambda|, & |E^2 - m^2 - 1| \leq 2m. \end{cases} \quad (\text{S60})$$

Combining with γ_A , the LE for different E is

$$\gamma_R = \begin{cases} \max \left\{ \ln \left| \frac{\lambda |E^2 - m^2 - 1| + \lambda \sqrt{(E^2 - m^2 - 1)^2 - 4m^2}}{m(|E| + \sqrt{E^2 - 4\lambda^2})} \right|, 0 \right\}, & |E| > 2\lambda \ \& \ |E^2 - m^2 - 1| > 2m, \\ \max \left\{ \ln \left| \frac{|E^2 - m^2 - 1| + \sqrt{(E^2 - m^2 - 1)^2 - 4m^2}}{2m} \right|, 0 \right\} > 0, & |E| \leq 2\lambda \ \& \ |E^2 - m^2 - 1| > 2m, \\ \max \left\{ \ln \left| \frac{2\lambda}{|E| + \sqrt{E^2 - 4\lambda^2}} \right|, 0 \right\} = 0, & |E| > 2\lambda \ \& \ |E^2 - m^2 - 1| \leq 2m, \\ 0, & |E| \leq 2\lambda \ \& \ |E^2 - m^2 - 1| \leq 2m. \end{cases} \quad (\text{S61})$$

For the energy interval in the second (third) row, since $|E^2 - m^2 - 1| > 2m$ ($|E| > 2\lambda$), it follows that $\gamma_R > 0$ ($\gamma_R = 0$). Therefore, the final LE of the system in real space is

$$\gamma_R = \begin{cases} \max \left\{ \ln \left| \frac{\lambda |E^2 - m^2 - 1| + \lambda \sqrt{(E^2 - m^2 - 1)^2 - 4m^2}}{m(|E| + \sqrt{E^2 - 4\lambda^2})} \right|, 0 \right\}, & |E| > 2\lambda \ \& \ |E^2 - m^2 - 1| > 2m, \\ \ln \left| \frac{|E^2 - m^2 - 1| + \sqrt{(E^2 - m^2 - 1)^2 - 4m^2}}{2m} \right|, & |E| \leq 2\lambda \ \& \ |E^2 - m^2 - 1| > 2m, \\ 0, & |E| > 2\lambda \ \& \ |E^2 - m^2 - 1| \leq 2m, \\ 0, & |E| \leq 2\lambda \ \& \ |E^2 - m^2 - 1| \leq 2m. \end{cases} \quad (\text{S62})$$

B. The LE of dual space

The eigenequation for dual space Hamiltonian (S53) is

$$\begin{aligned} t\psi_{b,k} + \lambda\psi_{a,k-1} + \lambda\psi_{a,k+1} &= E\psi_{a,k}, \\ t\psi_{a,k} + (J + me^{i(2\pi\alpha k + \theta)})\psi_{c,k} &= E\psi_{b,k}, \\ (J + me^{-i(2\pi\alpha k + \theta)})\psi_{b,k} &= E\psi_{c,k}. \end{aligned} \quad (\text{S63})$$

Similarly, one can simplify the eigenequations to the form with respect to the component ψ_a , i.e.,

$$\psi_{a,n+1} = \frac{E^3 - E(2m - 1 - t^2) - 2Em \cos(2\pi\alpha k + \theta)}{\lambda[E^2 - m^2 - 1 - 2m \cos(2\pi\alpha k + \theta)]} \psi_{a,n} - \psi_{a,n-1} \quad (\text{S64})$$

Then, one can directly obtain the corresponding transfer matrix

$$T_k = A_k B_k, \quad (\text{S65})$$

where

$$\begin{aligned} A_k &= \frac{1}{\lambda[E^2 - m^2 - 1 - 2m \cos(2\pi\alpha k + \theta)]}, \\ B_k &= \begin{pmatrix} E^3 - E(2m - 1 - t^2) - 2Em \cos(2\pi\alpha k + \theta) & -\lambda[E^2 - m^2 - 1 - 2m \cos(2\pi\alpha k + \theta)] \\ \lambda[E^2 - m^2 - 1 - 2m \cos(2\pi\alpha k + \theta)] & 0 \end{pmatrix}. \end{aligned} \quad (\text{S66})$$

Then, LE can be written as $\gamma_R(E) = \gamma_A(E) + \gamma_B(E)$, where

$$\begin{aligned} \gamma_A &= \lim_{N \rightarrow \infty} \frac{1}{N} \ln \prod_{k=1}^N \frac{1}{\lambda[E^2 - m^2 - 1 - 2m \cos(2\pi\alpha k + \theta)]} \\ &= \begin{cases} \ln \left| \frac{2}{\lambda(|E^2 - m^2 - 1| + \sqrt{(E^2 - m^2 - 1)^2 - 4m^2})} \right|, & |E^2 - m^2 - 1| > 2m, \\ \ln \left| \frac{1}{m\lambda} \right|, & |E^2 - m^2 - 1| \leq 2m. \end{cases} \end{aligned} \quad (\text{S67})$$

As for γ_B , we apply Avila's global theory on it, then one can get

$$\gamma_B = \begin{cases} \ln \left| \frac{|Em| + m\sqrt{(E)^2 - 4\lambda^2}}{2} \right|, & |E| > 2\lambda, \\ \ln |m\lambda|, & |E| \leq 2\lambda. \end{cases} \quad (\text{S68})$$

Combining with γ_A , the LE for different E is

$$\gamma_K = \begin{cases} \max \left\{ \ln \left| \frac{m(|E| + \sqrt{E^2 - 4\lambda^2})}{\lambda|E^2 - m^2 - 1| + \lambda\sqrt{(E^2 - m^2 - 1)^2 - 4m^2}} \right|, 0 \right\}, & |E| > 2\lambda \ \& \ |E^2 - m^2 - 1| > 2m, \\ \max \left\{ \ln \left| \frac{2m}{|E^2 - m^2 - 1| + \sqrt{(E^2 - m^2 - 1)^2 - 4m^2}} \right|, 0 \right\}, & |E| \leq 2\lambda \ \& \ |E^2 - m^2 - 1| > 2m, \\ \max \left\{ \ln \left| \frac{|E| + \sqrt{E^2 - 4\lambda^2}}{2\lambda} \right|, 0 \right\}, & |E| > 2\lambda \ \& \ |E^2 - m^2 - 1| \leq 2m, \\ 0, & |E| \leq 2\lambda \ \& \ |E^2 - m^2 - 1| \leq 2m. \end{cases} \quad (\text{S69})$$

Similarly, since the second (third) line of inequality satisfies $|E^2 - m^2 - 1| > 2m$ ($|E| > 2\lambda$), we have $\gamma_K = 0$ ($\gamma_K > 0$). The final LE for dual space is

$$\gamma_K = \begin{cases} \max \left\{ \ln \left| \frac{m(|E| + \sqrt{E^2 - 4\lambda^2})}{\lambda|E^2 - m^2 - 1| + \lambda\sqrt{(E^2 - m^2 - 1)^2 - 4m^2}} \right|, 0 \right\}, & |E| > 2\lambda \ \& \ |E^2 - m^2 - 1| > 2m, \\ 0, & |E| \leq 2\lambda \ \& \ |E^2 - m^2 - 1| > 2m, \\ \ln \left| \frac{|E| + \sqrt{E^2 - 4\lambda^2}}{2\lambda} \right|, & |E| > 2\lambda \ \& \ |E^2 - m^2 - 1| \leq 2m, \\ 0, & |E| \leq 2\lambda \ \& \ |E^2 - m^2 - 1| \leq 2m. \end{cases} \quad (\text{S70})$$

C. Mobility edge

Comparing the LE in the two dual spaces, one can find that the eigenstates in the region of $|E| \leq 2\lambda$ & $|E^2 - m^2 - 1| \leq 2m$ are delocalized in both spaces, which means they are actually the multifractal state. Moreover, the LE does not depend on the coupling parameter t . In other words, for arbitrarily small t , one can induce multifractal states in this lattice model. The ME between the extended and localized states is determined by the LE of the energy region with $|E| > 2\lambda$ & $|E^2 - m^2 - 1| > 2m$ for $E_c = \frac{m \pm \sqrt{m^2 + 4\lambda^2(m^2 + 1)}}{2\lambda}$.

TABLE IV. MMEs and quantum phases of partially-quasiperiodic lieb lattice

Quasiperiodic strength	$\lambda < (m + 1)/2$		$\lambda \geq (m + 1)/2$
Exact MMEs ($E_c =$)	$\pm 2\lambda$	$\frac{m \pm \sqrt{m^2 + 4\lambda^2(m^2 + 1)}}{2\lambda}$	± 2
Separated states	Ext.* and Mul.	Ext. and Loc.	Ext. and Mul.
Possible phases	Ext.+Loc., Ext+Mul.+Loc.		Loc.+Mul.

*Ext.=Extended states; Loc.=Localized states; Mul.=Multifractal states.

The LE versus E and λ is shown in Fig. S9(b).

In the first stage [$\lambda < (m + 1)/2$], the system has four MEs. Two are $E_c = \pm\lambda$ separating the extended and the multifractal state, the other two are $E = \frac{m \pm \sqrt{m^2 + 4\lambda^2(m^2 + 1)}}{2\lambda}$ separating the extended and the localized state.

In other words, though MMEs separating multifractal and localized states are not found in the first stage, this does not mean that the three-state coexisting quantum phase can not appear. As shown in Fig. S9(c), the IPR reflects that near $\lambda = 0.7$, three-state coexisting quantum phase emerges.

In the second stage [$\lambda \geq (m + 1)/2$], the region $-m - 1 \leq \frac{m \pm \sqrt{m^2 + 4\lambda^2(m^2 + 1)}}{2\lambda} \leq m + 1$ no longer satisfies the energy interval in the first line of Eq. (S62) and (S70). As a result, the MEs separating the extended and localized states

disappear. At this point the system enters a quantum phase in which the multifractal and the localized state coexist, separated by MMEs of $E = \pm 2$.

Finally, we summarize the MMEs and emergent quantum phases of the partially-quasiperiodic Lieb lattice in Tab. IV. The results again reveal that the system contains not only the traditional ME separating extended and localized states, but also the MMEs separating multifractal and localized states or separating multifractal and extended states. Meanwhile, exotic quantum phases featuring two-state coexistence (Ext. + Loc. or Loc. + Mul.) and three-state coexistence (Ext. + Mul. + Loc.) emerge.

This is yet another evidence supporting the conclusion: The MMEs and exotic quantum phases can emerge in the flat-band system.

VI. EXPERIMENTAL SCHEME OF THE PROGRAMMABLE RYDBERG ATOMIC ARRAY

Experimentally, one can realize the MMEs in diamond flat-band model by the following spin Hamiltonian

$$H_s = \sum_{j_x} (J\sigma_{j_x,A}^+ \sigma_{j_x,B}^- + J\sigma_{j_x,A}^+ \sigma_{j_x,C}^- + t\sigma_{j_x,A}^+ \sigma_{j_x,B}^- + J\sigma_{j_x+,B}^+ \sigma_{j_x+,A}^- + J\sigma_{j_x+,B}^+ \sigma_{j_x+,A}^- + \text{H.c.}) + \frac{1}{2} \sum_{j_x} V_{j_x} (\mathbb{I} + \sigma_{j_x,A}^z). \quad (\text{S71})$$

The above Hamiltonian can be transformed to the diamond quasiperiodic lattice by relabeling site index $j_x \rightarrow n$ for each leg and defining operator $b_n^\pm = |\uparrow\rangle_n \langle \downarrow|_n$ at each site, with $|\uparrow\rangle = 70P_{1/2}$ and $|\downarrow\rangle = 70S_{1/2}$ for ^{87}Rb atoms. We consider the three-legged superarray of Rydberg atoms, and each atom has been trapped in optical tweezers. The schematic diagram is shown in Fig. (a), where $R_1 = \frac{2R_y}{\sin\theta_A}$, $R_2 = \sqrt{R_1^2 + R_x^2 - 2R_1R_x \cos\theta_A}$, $R_3 = \sqrt{2R_1R_2 \cos(\theta_1 + \theta_2)}$ with R_x and R_y marked in the figure. From the sine and cosine theorems, we can further give the angle between the sublattice $\theta_1 = \pi - \theta_m - \theta_A$, $\theta_2 = \theta_m - \arcsin(\frac{R_1}{R_2} \sin\theta_A)$ and $\theta_3 = \theta_m - \arcsin(\frac{2R_1}{R_3} \sin\theta_A)$, where $\theta_m = 54.7^\circ$ is the magic angle.

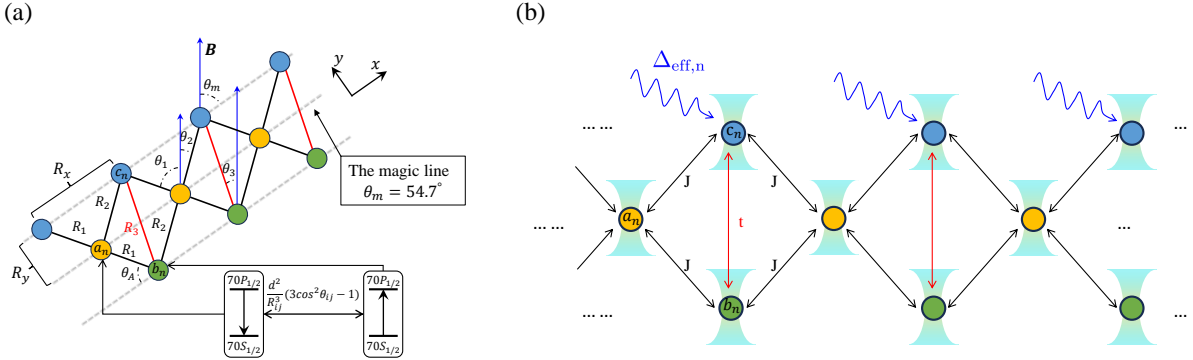


FIG. S10. Experimental scheme on MMEs of model (S7) in Rydberg atomic array. The corresponding angles are marked.

In fact, to realize the above Hamiltonian (S71) in Rydberg atomic array, angle-dependent dipole-dipole interactions and the AC Stark potential need to be realized successively, i.e., the total Hamiltonian of the experimental system reads

$$H = H_{dipole} + H_{AC}(r), \quad (\text{S72})$$

where the AC Stark term reads

$$H_{AC} = \sum_{j_x} \frac{|\Omega_0|^2}{\Delta} \cos^2(2\pi\alpha j_x) (\mathbb{I} + \sigma_{j_x,C}^z), \quad (\text{S73})$$

and the dipole-dipole term reads

$$\begin{aligned}
H_{dipole} = & \sum_{j_x} (J_{AB}\sigma_{j_x,A}^+\sigma_{j_x,B}^- + J_{AC}\sigma_{j_x,A}^+\sigma_{j_x,C}^- + J_{BC}\sigma_{j_x,B}^+\sigma_{j_x,C}^- + J_{BA}\sigma_{j_x,B}^+\sigma_{j_x+1,A}^- + J_{CA}\sigma_{j_x,C}^+\sigma_{j_x+1,A}^- + \text{H.c.}) \\
& + \sum_{|i-j|>1} \left(\frac{J_{ij}}{R_{ij}^3}\sigma_{i,A}^+\sigma_{j,B}^- + \frac{J_{ij}}{R_{ij}^3}\sigma_{i,A}^+\sigma_{j,C}^- + \frac{J_{ij}}{R_{ij}^3}\sigma_{i,B}^+\sigma_{j,C}^- + \text{H.c.} \right),
\end{aligned} \tag{S74}$$

where $\sigma^\pm = \frac{1}{2}(\sigma_x \pm i\sigma_y)$, σ_x and σ_y are the standard Pauli matrices. The dipole-dipole interaction between Rydberg atoms is given by $J_{ij} = \frac{d^2}{R_{ij}^3}(3\cos^2\theta_{ij} - 1)$, where d represents the transition dipole moment between the two Rydberg levels, R_{ij} with $i, j = A, B, C$ is the distance between sites i and j , and θ_{ij} is the angle between R_{ij} and the quantization axis defined by the magnetic field \mathbf{B} [36]. It is important to note that J_{ii} has been effectively mitigated to zero by selecting the angle θ_{ii} to be the magic angle, i.e., $\theta_m = 54.7^\circ$. Note that, the hopping term $J_{AB} = J_{AC} = J_{BA} = J_{CA} = J$ and $J_{BC} = t$, i.e., $\frac{d^2}{R_1^3}(3\cos^2\theta_1 - 1) = \frac{d^2}{R_2^3}(3\cos^2\theta_2 - 1) = J$ and $\frac{d^2}{R_3^3}(3\cos^2\theta_3 - 1) = t$. Since the latter non-nearest neighboring term decays with distance R_{ij}^3 , it can be safely ignored. Then, by setting values of any two of θ_A , R_x and R_y , the value of the third can be readily obtained by expressions $\frac{d^2}{R_1^3}(3\cos^2\theta_1 - 1) = \frac{d^2}{R_2^3}(3\cos^2\theta_2 - 1)$. For example, if we give $\theta_A = 50^\circ$, $R_x = 0.5a$, we get $R_y = 0.652a$. Then we obtain $J \propto 3.59d^2$ and $t \propto 0.66d^2$. If we discuss this in units of J , then $t/J = 0.184$.

The detailed steps of the whole experiment are as follows:

In the first step, the three-legged atomic array is prepared. We need to use optical tweezers, which is generated by spatial light modulator (SLM), to form ^{87}Rb atoms into a three-legged atomic array, so as to realize the flat-band quasiperiodic lattice [see Fig. (1) or Fig. (4) in the main text]. In concrete terms, we first grasp the atoms by optical tweezers, and then rearrange the atoms by an acousto-optical diffractometer (AOD). As a result, we have an ^{87}Rb atomic array in a two-dimensional plane as shown in Fig. (4).

The second step is to excite the atoms to Rydberg states. We excite the ^{87}Rb atoms from $5S_{1/2}$ state to $70S_{1/2}$. This step can be achieved through a two-photon process, i.e., coupling the $5S_{1/2}$ and $70S_{1/2}$ states through 420nm and 1012nm lasers (since the $6P_{1/2}$ state of the ^{87}Rb atoms has a relatively longer lifetime, we recommend using the $6P_{1/2}$ as the intermediate state during the two-photon process). Finally, the main part of MMEs experiment will be carried out on the two Rydberg states $70S_{1/2}$ and $70P_{1/2}$.

The third step is to shield the in-chain coupling. The magnetic field's magic angle shielding effect [36] is used to suppress the coupling between atoms in the same magic line.

The fourth step is to realize the quasiperiodic potential. Based on the AC stark effect, different sites can achieve an on-site potential that satisfies the quasiperiodic properties by shooting a 1012nm laser to the corresponding Rydberg atom (with a detuning of about 100MHz to the 1012nm Rydberg laser), i.e., $V_{AC} = V_{on-site} = \frac{|\Omega_0|^2}{\Delta} \cos^2(2\pi\alpha n)$. Specifically, this process can be carried out by introducing a second SLM. By generating a local controllable light shift, one can get site-dependent detuning $\Delta_{\text{eff},n}$ [marked in (b)], as Lukin's group recently reported [42, 43].

The fifth step is about evolution and measurement. One can excite one Rydberg atom to a superposition state of $70S_{1/2}$ and $70P_{1/2}$, i.e., $\frac{|0\rangle+|1\rangle}{\sqrt{2}}$ (see ref. [39]), and then let the system evolves for about $10\mu s$. The population of different Rydberg states can be measured by fluorescence image, and then one can obtain the wave function distribution of the system to determine whether the system is in an extended state, a localized state or a multifractal state.

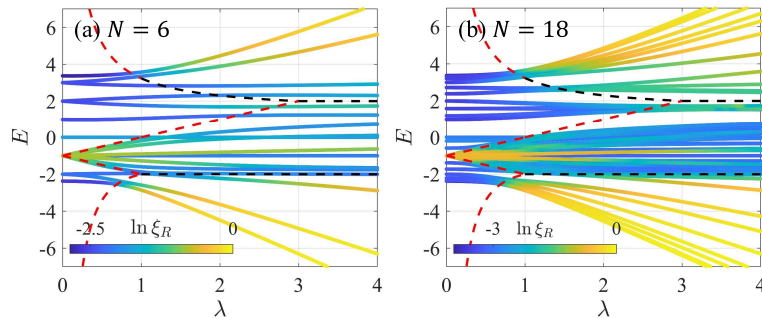


FIG. S11. The IPR phase diagrams for different system sizes. (a), (b) and (c) correspond to primitive cell number $N = 6$, $N = 10$, $N = 18$, respectively. The black (red) dashed line is the analytical MEs. In computation, we set $t = 1$ and $\lambda = 1.5$.

Fig. S11 shows the MEs at different system sizes. As can be seen from the figure, the larger the system is, the easier it is to observe MMEs and quantum phases. However, for all the flat-band model in this paper, we believe that 18 controllable Rydberg atoms (6 primitive cell) are enough to realize and observe the phenomena.

VII. THE MEASUREMENT SCHEME

VII-1. Basic principles

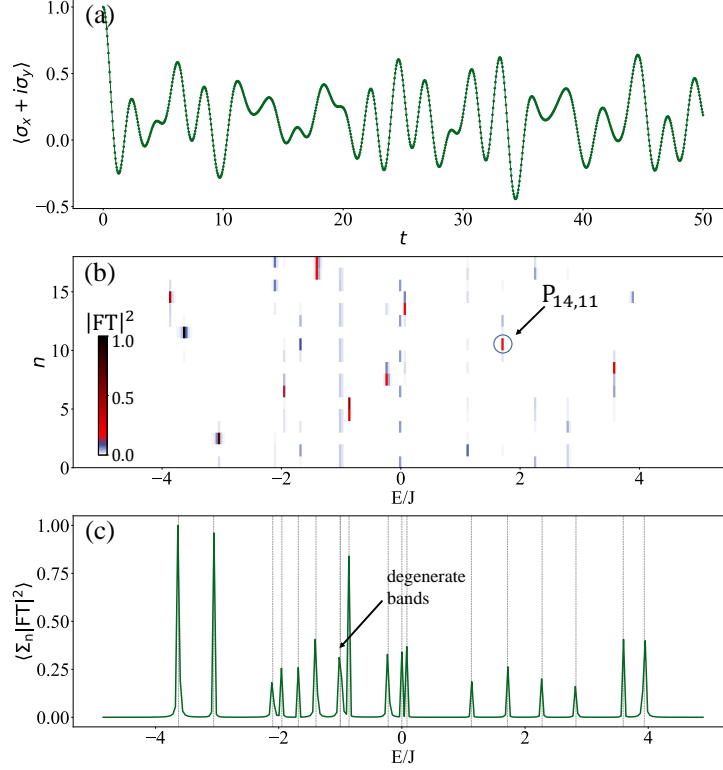


FIG. S12. (a) $\langle \sigma_n^+ \rangle$ versus time. (b) The Fourier transformation (FT) of $\langle \sigma_n^+ \rangle$ curves. $n \in \{1, 2, \dots, 18\}$ correspond to different initial states. The probability of a single spin-flip state on the 11-th site in the 14-th eigenstate $P_{14,11}$ is highlighted. (c) Average $|FT|^2$ amplitudes of the data in (b). Seventeen peaks emerge (contains a degenerate state). Throughout, $J = 2\pi \times 7.53\text{MHz}$.

Inspired by ref. [39], we propose in this Letter a measurement scheme based on the Rydberg atomic array, and the results predicted in this paper can be experimentally well observed. Taking 6 primitive cells (18 Rydberg atoms) as an example, we briefly describe the measurement process below.

According to the basic principles of quantum mechanics, the dynamics of a quantum system with time-independent Hamiltonian satisfies the Schrödinger equation. One can get the wave function versus time, i.e.,

$$|\psi(t)\rangle = e^{-iHt}|\psi(0)\rangle = \sum_{\alpha} C_{\alpha} e^{-iE_{\alpha}t} |\psi_{\alpha}\rangle, \quad (\text{S75})$$

where $\alpha \in \{1, 2, 3, \dots, N\}$ corresponds to the eigenvalue index. Through careful comparison, it is not difficult to find that the expression (S75) is similar to Fourier transform (FT). This means that one can use dynamical methods to extract the information of the eigenvalues and eigenstates.

Without loss of generality, a product state, i.e.,

$$|\psi(0)\rangle_n = \frac{1}{\sqrt{2}}(|\mathbf{Vac}\rangle + |\mathbf{1}\rangle_n) = |0\rangle_1 |0\rangle_2 \cdots \left(\frac{|0\rangle_n + |1\rangle_n}{\sqrt{2}} \right) \cdots |0\rangle_{N-1} |0\rangle_N \quad (\text{S76})$$

is selected as the initial state, where $|\mathbf{Vac}\rangle = |0\rangle_1 |0\rangle_2 \cdots |0\rangle_N$ denotes the vacuum state and $|\mathbf{1}\rangle_n = |0\rangle_1 |0\rangle_2 \cdots |1\rangle_n \cdots |0\rangle_N$ represents the single occupied Fork state (i.e., a single site spin-flip state).

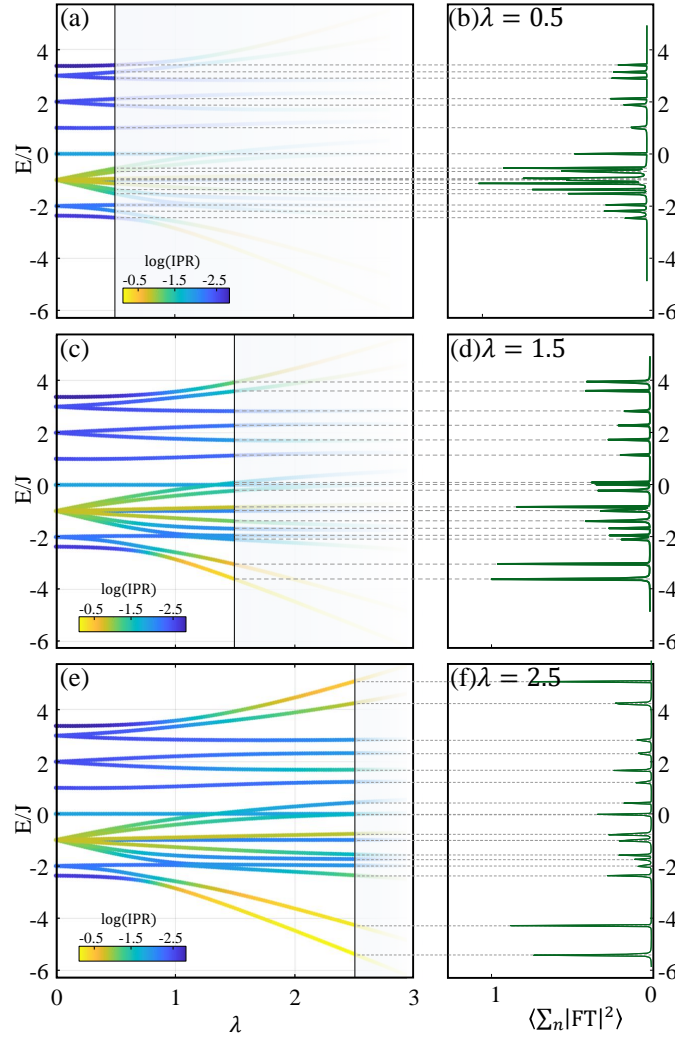


FIG. S13. The correspondence between the theoretically calculated eigenvalues of different quasiperiodic strengths in the IPR diagram and the eigenvalues extracted from numerical simulated experiments. Throughout, $J = 2\pi \times 7.53\text{MHz}$.

During the evolution process, by drawing the time evolution curve of $\langle \sigma_n^+ \rangle = \langle \sigma_n^x \rangle + i \langle \sigma_n^y \rangle$ [see Fig. S12(a)], and then conducting Fourier transform for the curve $\langle \sigma_n^+ \rangle$, one can obtain the modular square $|\text{FT}|^2$ for different frequencies α , which is denoted as $P_{\alpha,n}$ [see Fig. S12(b)]. In view of the correspondence relation between the evolution operator and the frequency amplitude of the Fourier transform, one can find that $|\text{FT}|^2$ is actually the superposition probability between the n -th site spin-up state and all eigenstates [39]. Furthermore, by allowing such single site spin-flip to traverse the entire atomic chain from $n = 1$ to $n = 18$, one can experimentally obtain all eigenvalues of the system [see Fig. S12(c)].

Through numerical experiments, we calculate the eigenvalues of 6 primitive cells under different quasiperiodic strengths, and the expected experimental results are shown in Fig. S13. We compare the energy predicted by the theory in the main text with the eigenvalues measured by numerical experiments at different quasiperiodic strength $\lambda = 0.5, 1.5, 2.5$. From Fig. S13, one can find that the experimental scheme of eigenenergies' measurement works well.

VII-2. Experimental measurements of the IPRs

After obtaining all the $P_{\alpha,n}$'s values, one can directly obtain the corresponding IPR ξ that reads

$$\xi_R(E_\alpha) = \sum_n P_{\alpha,n}^2. \quad (\text{S77})$$

Fig. S14 shows the concrete situation of IPR results.

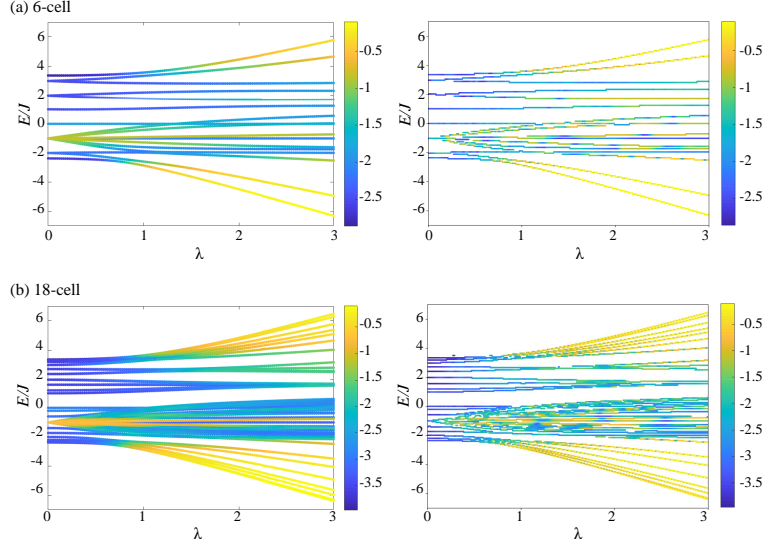


FIG. S14. Comparison of IPR between theoretical calculation (the left column) and numerical simulated experiments (the right column) for the case of 6 (a) and 18 (b) unit cells. Under the condition of the principal quantum number equals to 70, the energy unit $J = 2\pi \times 7.53\text{MHz}$.

First, taking a close look at the 6 primitive cells as shown in the figure, one can find that the theoretical results agree perfectly well with that of the numerical experiments. However, in the process of adjusting the quasiperiodic strength, there appear some regions with very small energy intervals, and even cases of energy degeneracy. This makes it very difficult to distinguish eigenstates of similar energies. In other words, the energy resolution requirement for detection is very high, which poses a challenge to experiment. With the current most advanced Rydberg experimental platforms, such as setups of Prof. Browawy's group or Prof. Lukin's group, the array of 18 Rydberg atoms required here can be readily achievable [43, 45, 46].

Besides, we also show the IPR results of the 18 primitive cells (54 Rydberg atoms). In principle, the greater the number of atoms, the lower the demand for the measurement accuracy. In other words, for example, we fix a set of $\{\lambda, E\}$ to measure the corresponding IPR. The more Rydberg atoms, the more points around this data point. All points in a region with the same localization properties (an extended, localized, or multifractal region) share the same wave function properties. If there are many eigenvalues densely distributed in the region, generally, the correct IPR can be measured even if operation errors occur in the experiment process. However, if the atomic array is too small in size, probably there will no well-defined points near the measuring point, which will lead to errors in the measurement results.

VII-3. Experimental measurements of the LEs

From the results of $P_{\alpha,n}$, one can directly obtain the corresponding eigenstates and LEs. Since the localized state wave function always satisfies the following expression, i.e.,

$$\psi_{R/K} \propto \max\{P_{\alpha,n}\} e^{-\xi(n-n_0)}, \quad (\text{S78})$$

where $\max\{P_{\alpha,n}\}$ is the maximum amplitude with a fixed α . n_0 is the site corresponding to the maximum amplitude.

One can select an arbitrary point with fixed disorder strength and energy parameters in the localized phase region, where the corresponding eigenstates always exhibit localization properties in real space and extension properties in dual space. Similarly, wave function in the extended phase shows the extension property in real space and the localization property in dual space. Multifractal states are in between. In concrete terms, the wave function exhibits partial expansion in both real space and dual space. Note that, multifractal wave function is not sufficiently extended compared with the standard extended state.

Based on the above properties, the first step in the experiment is to measure the specific configuration of the wave function. Then the wave function is fitted with exponential function to extract the corresponding Lyapunov exponents (S78). We obtain the predicted experimental results by numerical simulation using the dynamical method described in the previous subsection [see Fig. S15 and Fig. 4 in main text].

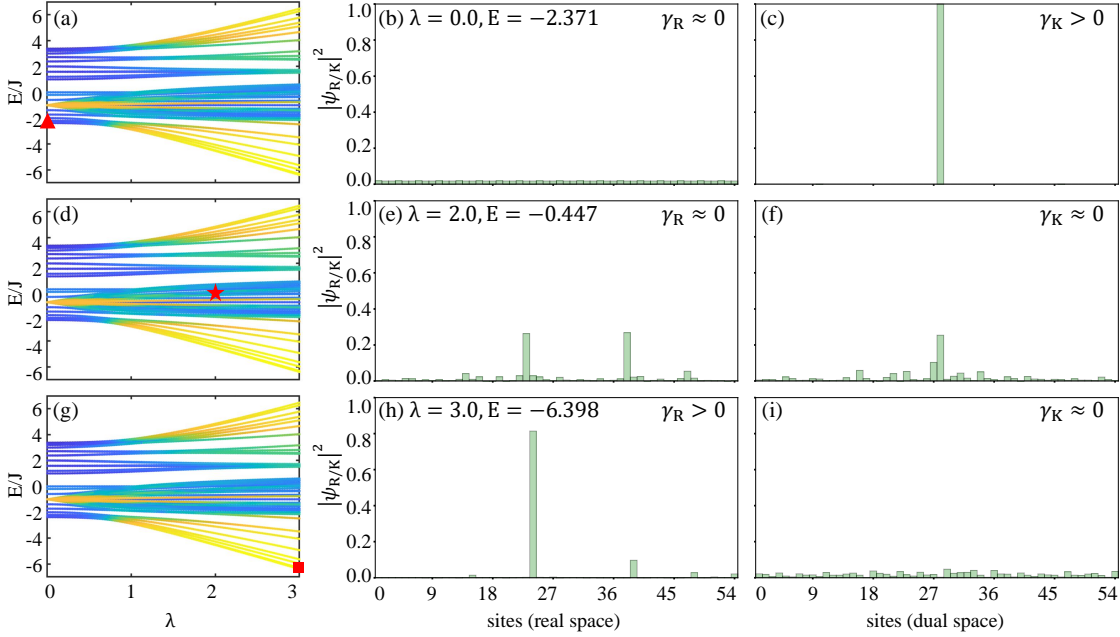


FIG. S15. Numerical experiments to measure LEs in the system with 18 unit cells. From top to bottom, the results correspond to the cases of extended, multifractal and localized states, respectively. Throughout, $J = 2\pi \times 7.53\text{MHz}$.

As shown in Fig. S15, selecting three parameter points (triangle, star, square) in different phase regions, one can obtain wave functions of extended, multifractal and localized states, respectively. Comparing the 6 unit cells' results (Fig. 4 in main text), one can find that there is an unavoidable scale effect in the system. Therefore, in experiments, if other factors are not considered, the larger the system, the better the results. However, given the current number of controllable qubits in Rydberg atomic arrays, one cannot demand too much of the experimental accuracy. In this connection, 6 unit cells selected system is good for the rough observation of relevant phenomena. Here, in order to compare with the theoretical results, we still retain the dimensionless data in the figure, and the parameters required by the specific experiment can be converted according to the value of J . In addition, the energy coordinates in the specific experiment need to be rescaled with the lowest energy being the zero point.

Furthermore, in principle, multifractal wave functions should exhibit multifractal structures, that is, a self-similar structure. Again, because of the size effect, neither 6 unit cells nor 18 unit cells can capture the multifractal structure well. If we assume that one can have 432 unit cells (1296 Rydberg atoms), the wave function will see a multifractal structure (see Fig. S16).

At last, with the current technology, the high requirement for control accuracy of energy and quasiperiodic intensity pose a real challenge to experimental physicists [39, 43, 45, 46]. We hope that more mature techniques of large-scale atomic array in the future will make the above interesting results easier to observe. Since the theory proposed in this Letter is universal, we also hope that the phenomena predicted here can be realized in other quantum simulators (such as trapped ions [47], IBM quantum processors [48], etc.).

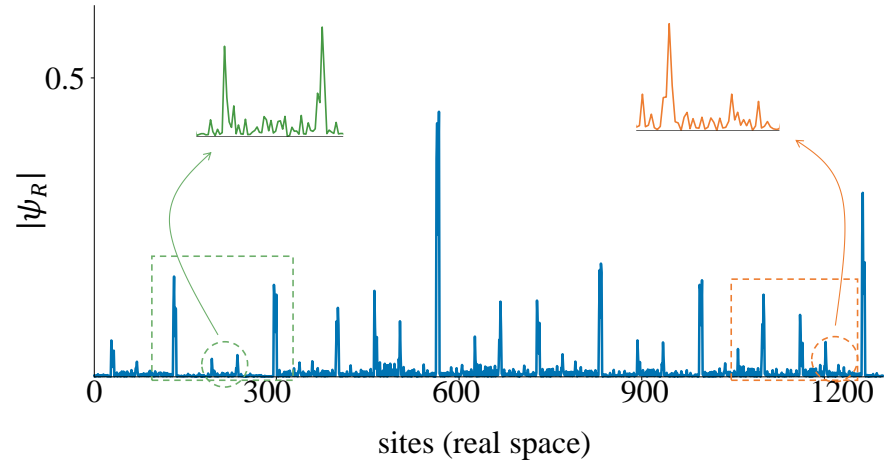


FIG. S16. Self-similar structure of a multifractal wave function. The system contains 432 unit cells.